TECHNISCHE UNIVERSITÄT WIEN
Vienna University of Technology

universität innsbruck

photonik
photonics

Masterthesis

Optical Characterisation of Quantum Dots embedded in Micropillars

by

Daniel Föger, BSc.

submitted in partial fulfilment of the requirements
for the degree of

Master of Science (MSc.)

Supervisor: Univ. Prof. Gregor Weihs
Co-Supervisor: Univ. Prof. Thorsten Schumm

Innsbruck, March 2013

Abstract

In this thesis I focus on various methods for a theoretical and experimental characterisation of InAs quantum dots embedded in micropillars. My thesis is structured as follows:
In the first chapter an introduction and a motivation for the fundamental research with quantum dots in micropillars is provided. Chapter 2 contains a basic description of self-assembled InAs quantum dots, their fabrication process as well as an overview of their physical properties. In the third chapter micropillars are described. At the end of this chapter a powerful method for the simulation of eigenmodes of micropillars is presented. Chapter 4 provides a short overview of the photon statistics of different light sources and introduces the second-order correlation function.
Chapter 5 summarizes the experimental work of my thesis. It can be organized into three parts, in which the first provides an overview of our experimental setup. The second part describes the basic measurements for an optical characterisation of quantum dots in micropillars and the third presents the most important experimental results.
A conclusion and an outlook at the end of my thesis provide a short summary of the major achievements and describe projects of our research group in the near future.

Contents

Chapter 1

Introduction

Nowadays semiconductor nano technology is widely spread and commonly used in everyday life. Almost everybody is used to its applications and possibilities and most of the time we do not consider that those technologies originally have been discovered and developed by experts in a laboratory environment. These days the evolution of modern semiconductor technology has to cross a borderline due to the quantum effects that appear at very small dimensions.
Quantum theory originated in the early 20^{th} century, when M. Planck and A. Einstein postulated the photon as an elementary light particle [1, 2]. This theory has come a long way since then and has yielded many important concepts and applications.
To get a connection between modern semiconductor technology and quantum theory the study of semiconductor quantum optics has become a very interesting topic of research. Semiconductor devices as solid state systems are easily scalable and therefore ideal for the integration on a chip. Especially semiconductor quantum dots are very interesting candidates which show single atom like behaviour despite being a solid state system. Quantum dots have discrete energy states which result in sharp spectral lines for emission and absorption. Furthermore, quantum dots produce nonclassical light [3] and can also generate entangled photons [4]. These are the basic elements for various schemes in quantum optics like quantum cryptography [5], quantum computing [6], and quantum teleportation [7].
The goal of embedding quantum dots into micropillars is to design an addressable source of directed nonclassical light. Furthermore micropillars act as high quality microresonators and therefore the emissionrate of distinct quantum dot transitions can get enhanced [8].

Chapter 2

Semiconductor Quantum Dots

A semiconductor quantum dot is a very small region (typically a few nm wide) inside a semiconductor in which electrons from the conduction band, holes (missing electrons from the valence band), or both can be trapped. Due to the small size of this region the possible energies for the trapped particles are quantized [9]. In our experiments we use semiconductor heterostructures as quantum dots. Nowadays the fabrication of structures with confinement of charge carriers in one dimension (quantum wells), two dimensions (quantum wires), or three dimensions (quantum dots) are possible. Figure 2.1 illustrates the influence of spatial confinement to the density of states.

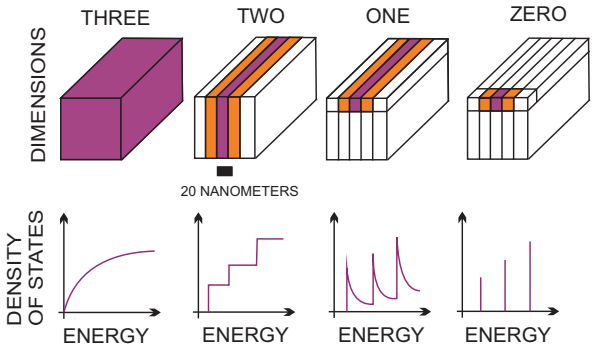

Figure 2.1: The density of states inside a very small semiconductor material is massively dependent on the size of the structure. For a so called "zero-dimensional" structure the energy-levels of the charge carriers are discrete. Image from [10].

In general to be able to trap electrons as well as holes a lower bandgap material is embedded in between a wider bandgap material. For optically active quantum dots a type-I bandgap discontinuity is needed. Type-I means that the

bandgap of one semiconductor is completely contained in the bandgap of the other material. The generation of optically active quantum dots also requires a direct band gap semiconductor as the lower bandgap material. Some material pairs are for example InAs/GaAs, InP/GaInP, and GaN/AlGaN (III-V) and CdSe/ZnS (II-VI) [3]. In these systems the recombination of the charge carriers inside the quantum dot can be observed directly in the optical spectrum. In our experiments we work with self-assembled InAs/GaAs quantum dots.

2.1 Fabrication of Self-Assembled InAs Quantum Dots

Self-assembled InAs/GaAs quantum dots are produced through molecular-beam epitaxy (MBE). First a substrate with a GaAs surface is placed in vacuum and heated. The pure solid elements (In and As) are heated and the atoms are deposited onto the surface of the substrate. With this technique it is possible to deposit single atomic layers onto the substrate. Figure 2.2 shows the growth process of quantum dots using MBE. After a critical thickness of the InAs layer it is energetically favourable for InAs to form small islands. Those small islands are the quantum dots. They are randomly distributed on the GaAs surface. Dependent on the growth parameters InAs quantum dots are 4-7 nm thick and 20-40 nm wide [3].

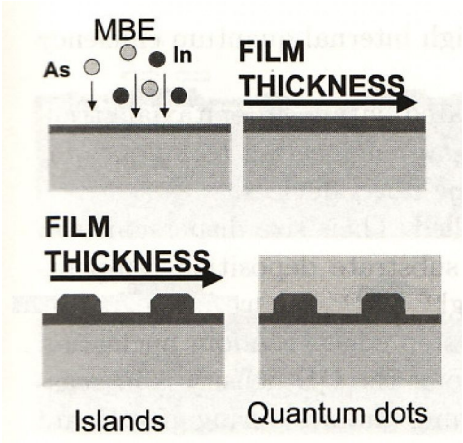

Figure 2.2: InAs is deposited onto a GaAs surface with molecular-beam epitaxy. The lattice mismatch of 7% [3] between the two different materials results in the formation of small InAs islands. A thin layer of InAs (only a few monolayers) remains on the surface. This layer is called wetting layer and it is able to confine charge carriers in one dimension. This quantum well behaviour is also visible in the optical spectrum, see figure 2.7. After this formation, GaAs is deposited onto the sample. The low bandgap InAs structure is then completely surrounded with the higher bandgap GaAs. Graphics taken from [11]

2.2 Physics of Quantum Dots

In general, the optical as well as the electronic properties depend heavily on the geometry and the material composition of the quantum dot. Mainly responsible for the size and the composition is the growth process. Although the position of a quantum dot is random with MBE growth, one can control the density and the size of the quantum dots by choosing the amount of deposited material. Also the growth rate and the process temperature are very important parameters which have a major influence on the physical properties of semiconductor quantum dots.
Due to the discrete energies of charge carriers inside a quantum dot the solid state system shows atomic-like properties. These properties give rise to a shell model for carrier energy levels inside the quantum dot (s-, p-, d-shell). The shell structure was first observed by using capacitance (C-V) and infrared spectroscopy measurements on InAs/GaAs quantum dots in 1994 [12].

2.2.1 Electronic Properties of Quantum Dots

Charge carriers are confined inside quantum dots due to their small dimensions. This confinement generates discrete energy levels, which can be approximately calculated by choosing a suitable confining potential and solve the Schrödinger equation for a bound particle.

$$H\psi(r) = \left(-\frac{\hbar^2}{2m^*}\nabla^2 + V(r)\right)\psi(r) = E\psi(r) \tag{2.1}$$

As a very simple but quite far reaching example one could calculate the bound states of the quantum dot by applying a symmetrical potential. This model will be described in this section (adapted from [3]). Since self-assembled InAs quantum dots have a small height and a relative large lateral expansion, one can choose an infinite square well potential in z direction and a harmonic potential in lateral directions.

$$V(r) = \begin{cases} \frac{1}{2}m^*\omega_0(x^2+y^2) & |z| < \frac{L}{2} \\ \infty & |z| > \frac{L}{2} \end{cases} \tag{2.2}$$

L describes the height of the quantum dot, m^* the effective mass of the confined charge carrier respectively and ω_0 the level spacing of the lowest states.

The energy levels resulting from this calculation with the chosen Hamiltonian are:

$$E(n_x, n_y, n_z) = (n_x^2 + n_y^2)\hbar\omega_0 + \left(\frac{\pi^2\hbar^2}{2m^*L^2}\right) n_z^2 \tag{2.3}$$

n_x and n_y refer to integers larger or equal to zero. n_z could be any integer larger than zero. Due to the small height of an InAs quantum dot, a variation of n_z would cause a very large shift in the energy. Therefore n_z is basicially set to one, when describing the lowest order energy levels. A schematic of these energy levels as a function of their quantum numbers, $E(n_x, n_y)$ is shown in figure 2.3. In figure 2.4 we plotted the recombination energy from the electron ground state and the hole ground state in a quantum dot versus the height of the quantum dot.

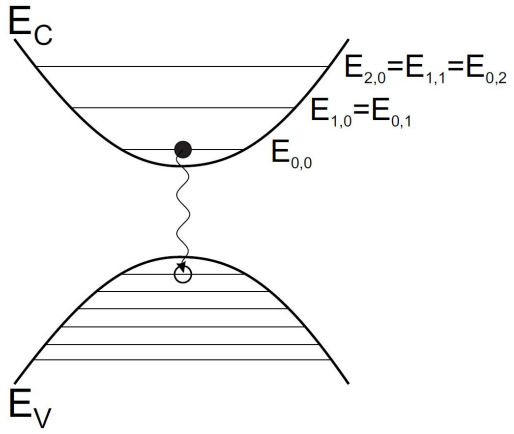

Figure 2.3: The solution of the Schrödinger equation with an infinite square well potential in z direction and a harmonic potential in lateral directions yields equidistantly separated energy levels for electrons and holes, respectively. The recombination process from the electron ground state to the highest hole state is schematically drawn. Image from [3].

In general, quantum dots can capture multiple charge carriers. If more charged particles are confined inside the quantum dot, one has to take the interaction between these charge carriers into account to explain the electronic properties. In figure 2.5 several different quantum dot states are shown. Due to the broken rotation symmetry of the quantum dot structure also finestructure-splitting of the quantum dot states is present [13].

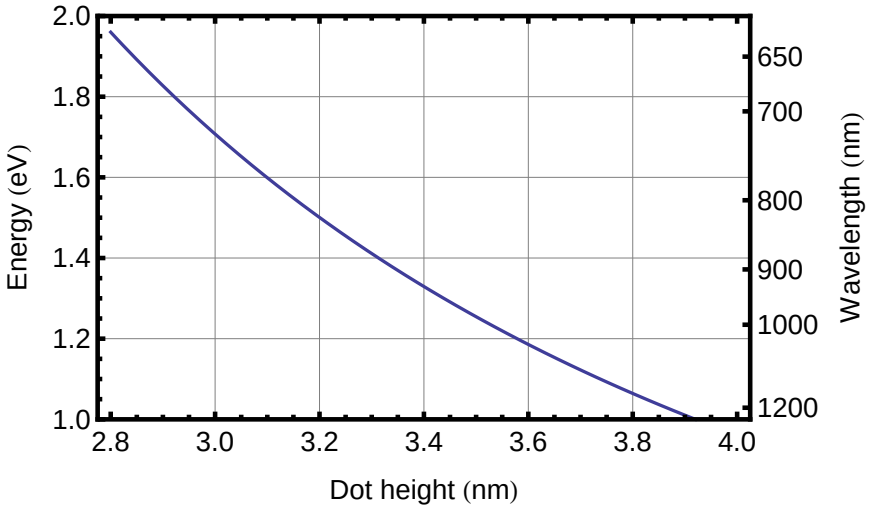

Figure 2.4: The calculated energies and wavelengths of the recombination process from the electron ground state to the hole ground state versus the quantum dot height. For the calculation equation (2.3) and the parameters $0.41 \cdot m_e$ for the effective hole mass and $0.023 \cdot m_e$ for the effective electron mass were used [14]. For our experiment we expect a quantum dot height of approximately 3.4 nm, because the s-shell transition of our quantum dots is approximately at 920 nm.

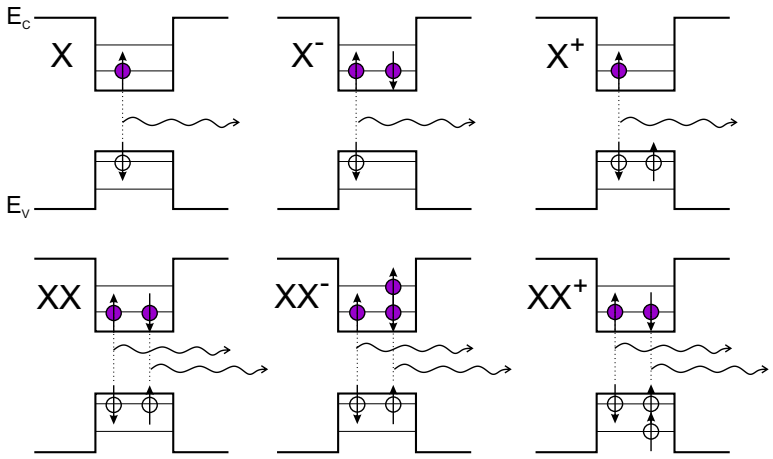

Figure 2.5: Several different quantum dot states and their recombination processes. The first picture on the top left describes an exciton state (X). The one next to it refers to a negative charged exciton (trion-X^-). The top right picture corresponds to a positive charged exciton (trion-X^+). The bottom picture on the left side describes a biexciton (XX). The images next to it refer to a negative and positive charged biexciton, (XX^-) and (XX^+) respectively. Illustration from [15].

2.2.2 Optical Properties of Quantum Dots

The optical excitation of quantum dots can be performed on resonance with their emission or above the GaAs bandgap (above 1.52 eV or below 817 nm, respectively). The above band excitation generates electron-hole pairs in the surrounding of the quantum dot. Those charge carriers underlie different intraband relaxation processes and can get trapped inside the quantum dot. The main relaxation mechanism is thought to be phonon emission [16]. If the carrier density is higher, also Auger processes can contribute [3].

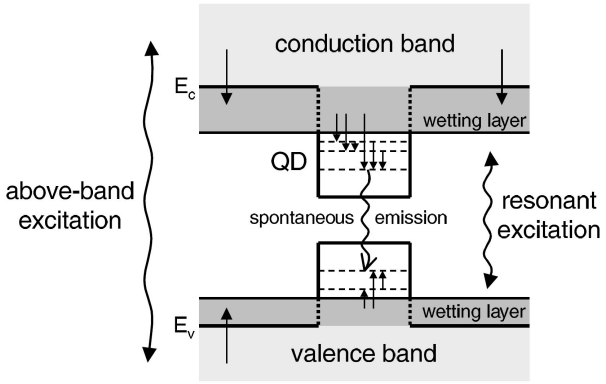

Figure 2.6: The energy-regimes of an InAs quantum dot embedded in GaAs, from [3]. Since InAs quantum dots have energy levels between the bandgap of GaAs the quantum dot has an attractive potential for electrons as well as for holes.

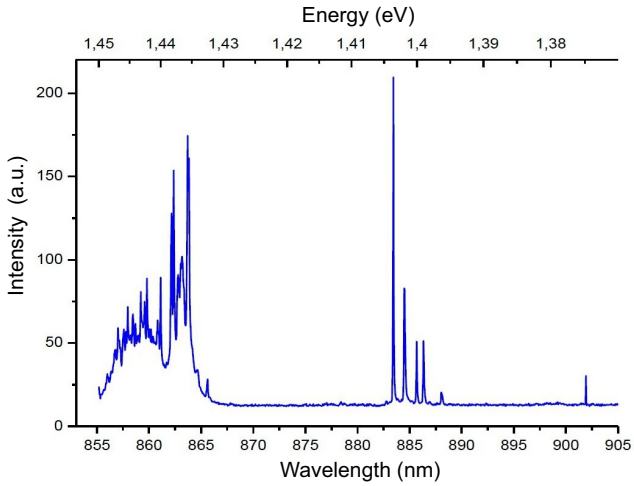

Figure 2.7: Spectrum of an InAs quantum dot (sharp lines around 885 nm) and the emission from the wetting layer (broad signal from 855 nm to 865 nm).

The advantages of the above band excitation are that no scattered laser light is present at the wavelength of the quantum dot emission. Furthermore one can investigate all energy regimes of the structure, the wetting layer, the emission from the quantum dots and also the direct recombination from the GaAs bandgap. The process itself is also quite efficient, because a large area of the GaAs material is used as an absorber. Therefore only a few $\mu W/\mu m^2$ of laser intensity are needed.
Under resonant excitation usually higher quantum dot states (e.g. p, d-states) are populated. These states decay and populate the lower quantum dot states. The main advantage of this excitation scheme is that charge carriers are directly created inside the quantum dot and therefore the single photon emission process does not suffer from delay effects due to the trapping mechanism. Since quantum dots have a small cross section the laser intensity has to be sufficiently higher (up to a few $mW/\mu m^2$). With resonant excitation also the probability of creating charged states inside the dot can be lowered. By applying a resonant excitation scheme Rabi oscillations from the quantum dot emission should be visible [3]. However, because of incoherent relaxation processes inside the quantum dot and from the surrounding it is very hard to observe them. In figure 2.6 the energy regime which is used for resonant excitation is drawn. A possible way to get rid of many incoherent internal processes is to use a resonant two photon excitation scheme which is shown in figure 2.8.

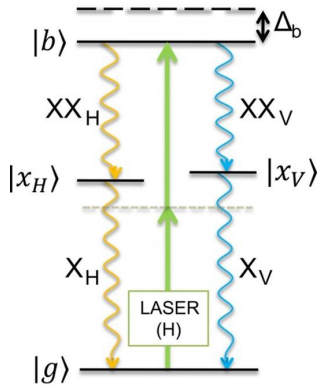

Figure 2.8: Resonant excitation by using a two photon absorption process. The transition from the ground state to the biexciton state is driven by a resonant two photon process using a virtual level.

2.3 Distributed Bragg Reflectors

Most of our quantum dot samples are sandwiched between two distributed Bragg reflectors (DBR). A DBR consists of alternating layer pairs of high and low refractive index material (e.g. AlAs and GaAs). The layers have in general a

thickness of a $\lambda/4$ (λ is the design wavelength of the cavity). Due to constructive interference, the two DBRs are high reflectance mirrors [17]. The range of wavelengths that is reflected is called the stopband, see figure 5.12. If there is a $n \cdot \lambda/2$ ($n \in \mathbb{N}$) thick central layer present between the two DBRs forming a Fabry-Perot cavity, the structure shows a resonance for transmission in the middle of the stopband. The reflectivity spectrum of a planar DBR can be simulated by using a transfer-matrix method [18]. The refractive index of a material in general depends on the temperature [19]. For our resonator materials (GaAs and AlAs) the reflectivity spectrum of the resonator gets blue shifted if the temperature is decreased. D. Burak and R. Binder proposed a method for simulating vectorial eigenmodes of VCSEL's (Vertical-cavity surface-emitting laser) [20]. This method was used for simulating the reflectivity spectrum of micropillars, see section 3.3 for further details.

2.4 Quantum Dot Samples

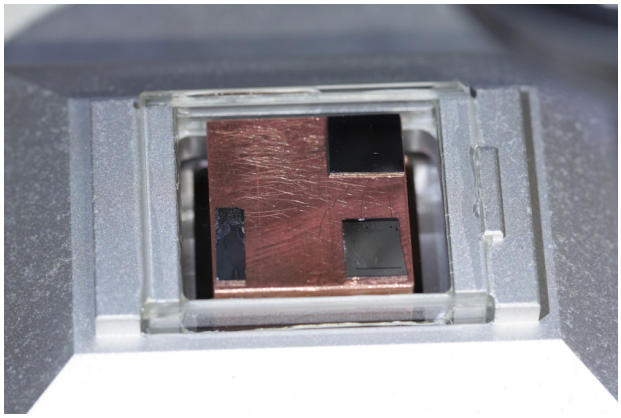

Figure 2.9: This picture shows three samples which were used in the experiments described in this thesis. The wafers are on the copper coldfinger of the cryostat. The top right is sample #m649 (section 2.4.1), the bottom left is the micropillar sample C3281 (section 3.4.1) and the bottom right is the calibration sample C3281-13,7 (section 2.4.2).

2.4.1 Sample #m649

This sample was grown by G. Solomon at the Joint Quantum Institute of the National Institute of Standards and Technology at the University of Maryland. A planar DBR cavity consisting of 15.5 lower layer pairs and 10 upper layer pairs of AlAs and GaAs is present on the sample. The cavity resonance is at 919.4 nm. Within the central layer a low density of self assembled InAs quantum dots (approximately 10 μm^{-2}) are embedded. The InAs quantum dots were grown

by MBE at 495 °C and their s-shell emission lies close (approximately ±5 nm) to the cavity resonance. The central layer also offers waveguideing properties and therefore the quantum dots can be excited from the side as well, see section 5.1.

2.4.2 Calibration Sample C3281-13,7

The sample C3281-13,7 was produced at the University of Würzburg by C. Schneider. The main aim for characterising this sample was to control the results of the InAs quantum dot growth process in terms of quantum dot density and biexcitonic emission. The top DBR of this sample therefore has been removed (two remaining mirror pairs) and a shadow mask was processed on top. Holes with different diameters (from 0.2 μm to 4 μm) were etched into the mask which allow to observe areas of the central layer with different sizes. The results are discussed in chapter 5.

The micropillar samples C3281 and M4792 are discussed in chapter 3 in section 3.4.

Chapter 3

Micropillars

Nowadays many research activities concentrate on the realization of microresonators with high quality factors. The study of cavity electrodynamics is a fast growing field of science which also has a huge potential for future applications. Light confinement on the length scale of the photon wavelength can be achieved inside a microcavity with a wavelength-thick central layer (GaAs), which is sandwiched between an upper and a lower DBR. This confinement yields to many well observable quantum effects. To realize addressable single photon sources, microscopic lasers or for investigating the underlying physical laws often a layer containing quantum dots is introduced into to the middle of the central cavity layer. Furthermore the enhancement of distinct quantum dot transitions due to the Purcell effect [8] in these microresonators offers a chance for manipulating the lifetime of certain quantum dot states.

3.1 Fabrication and Theoretical Background

Typically, micropillars are grown by molecular beam epitaxy. In our case the DBR layers consist of alternating $\lambda/4$-thick layers of AlAs and GaAs. Quantum dots are embedded in the central one λ-thick GaAs layer. After the growth of this planar cavity, micropillars are produced by electron-beam-lithography and reactive ion etching.

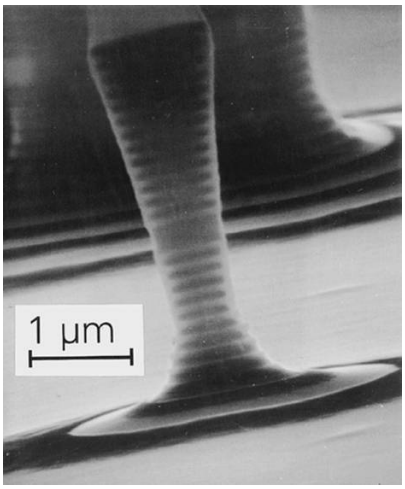

(a) Scanning electron microscope picture of an early quantum dot micropillar. This picture was taken in 1996, from [21].

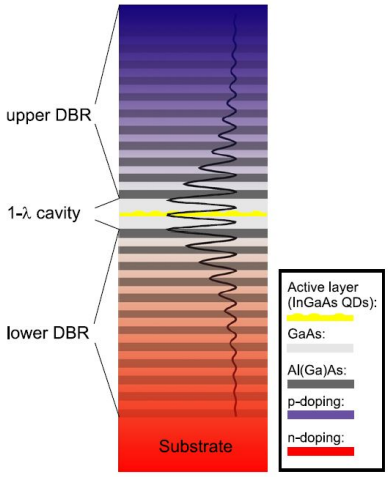

(b) Profile from an Al(Ga)As/GaAs microcavity structure from [22]. The quantum dot layer is positioned inside the central GaAs layer exactly at an antinode of the cavity mode to guarantee a maximum light-matter interaction. To electrically excite the quantum dot one can use a diode-like structure,with n- and p-doped areas, respectively.

Figure 3.1: (a) Scanning electron microscope (SEM) image and (b) a schematic profile of a micropillar.

Very important parameters for a microresonator are its quality factor Q and its mode volume V_m. The quality factor is defined by the ratio between the emission energy E_c of the fundamental cavity mode and its linewidth γ_c (FWHM). A small mode volume generates a high vacuum field inside the cavity, because of $E_{vac} \; \alpha \; \sqrt{\frac{1}{V_m}}$. The coupling strength between the cavity and the quantum dot emission is linearly depended on the size of its vacuum field, so the mode volume of the microresonator should be minimized [22].

The quality factor of a cavity basically describes the lifetime of photons inside the cavity. Losses e.g. transmission, scattering, or absorption of photons result in a shortened lifetime. Therefore the coupling strength between the cavity and the quantum dot emission depends directly on the Q-factor of the cavity. For high quality microcavities the Q-factor can be expressed by equation (3.1) [23, 24]:

$$1/Q = 1/Q_{\text{intrinsic}} + 1/Q_{\text{edgescattering}} + 1/Q_{\text{absorption}} \tag{3.1}$$

This equation claims that losses are additive. $Q_{\text{edgescattering}}$ and $Q_{\text{absorption}}$

can be approximately calculated by:

$$1/Q_{\text{absorption}} = 4\pi n/\lambda_c \alpha_M \tag{3.2}$$

$$1/Q_{\text{edgescattering}} = \kappa J_0^2(k_t R)/R \tag{3.3}$$

λ_c describes the resonance wavelength, n the refractive index and α_M refers to the absorption coefficient of the material. The losses due to edge scattering are proportional to fundamental mode intensity $I(R)$ at the micropillar edge divided by the micropillar radius R [23]. By neglecting longitudinal field components, we can assume $I(R) \propto J_0^2(k_t R)$, in which J_0 is the zeroth Bessel function of first kind and k_t refers to the transversal wavevector with $k_t = \sqrt{nk_0^2 - \beta^2}$ [23]. β is the mode propagation constant (here, the longitudinal component of the wavevector) and nk_0 is the wavenumber within the material. Section 3.3 provides a closer look into the propagation and confinement of electromagnetic radiation inside a micropillar. κ refers to a phenomenological proportionality constant.

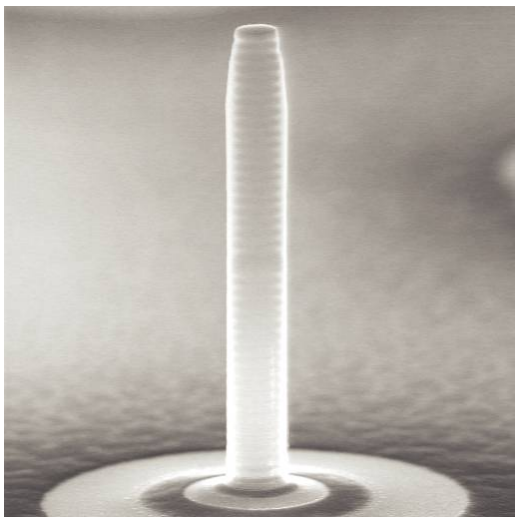

Figure 3.2: A state of the art micropillar with a diameter of 1 μm. This structure was produced by J. P. Reithmaier et al. in 2004. Picture from [25].

The intrinsic Q-factor of a micropillar depends on the number of mirror pairs (the thickness of the DBR structure), which determines the internal reflectivity of the cavity. In [26] the intrinsic Q-factor of a planar microcavity is calculated by using:

$$Q_{\text{intrinsic}} = \frac{2L_{\text{eff}}}{\lambda_c} \frac{\pi}{1 - r_l r_u} \tag{3.4}$$

λ_c is the resonance wavelength. L_{eff} refers to the effective cavity length, which is approximately $n_{\text{cav}} d_{\text{cav}} + 2n_{\text{eff}} L_m$, where n_{cav} is the refractive index for

the cavity layer, d_{cav} the thickness of the cavity layer, L_m the effective mirror length and n_{eff} the effective refractive index for the mirror. The effective refractive index for DBR-layers with the same optical path-length is given by $n_{\text{eff}} = 2n_{\text{GaAs}}n_{\text{AlAs}}/(n_{\text{GaAs}} + n_{\text{AlAs}})$. The effective mirror length can be calculated by $L_m = m_{\text{eff}}(d_{\text{GaAs}}+d_{\text{AlAs}})$. d refers to the thickness of the corresponding layer and m_{eff} is the effective number of mirror pairs "seen" by the wave electric field. For thick DBRs ($m \to \infty$) m_{eff} is given by $1/2(n_{\text{GaAs}} + n_{\text{AlAs}})/(n_{\text{GaAs}} - n_{\text{AlAs}})$, [27]. m refers to the number of mirror pairs. r_l and r_u are the reflectivity of the lower and upper DBR region, respectively. The reflectivity for the upper and the lower mirror can be calculated using, [27]:

$$r = \frac{n_0 - (n_{\text{AlAs}}/n_{\text{GaAs}})^{2m}}{n_0 + (n_{\text{AlAs}}/n_{\text{GaAs}})^{2m}} \tag{3.5}$$

where n_0 is the refractive index of the material after the DBR which is 1 for the upper and n_{GaAs} for the lower mirror.
One way to characterise the coupling strength between the cavity and the quantum dot emission is to use the Purcell factor. The rate of spontaneous emission of a light source is dependent on its environment. If an emitter is located inside a cavity and its emission is on resonance with the cavity mode, there is an enhanced light coupling to the cavity mode present. In this case the spontaneous emission lifetime of the emitter decreases because of the higher light coupling [8]. The Purcell factor is the ratio between the undisturbed lifetime and the maximally shortened lifetime of an emitter in a resonator:

$$F_P = \frac{\tau_{\text{Bulk}}}{\tau(\Delta = 0)} \tag{3.6}$$

τ_{Bulk} is the spontaneous emission lifetime of the emitter in bulk material without the presence of the resonator. $\tau(\Delta = 0)$ refers to the lifetime of the emitter on resonance (detuning Δ equal zero).
Another approach for the Purcell factor shows the dependence on the quality factor and the mode volume of the resonator [28]:

$$F_P = \frac{3}{4\pi^2}\left(\frac{\lambda_c}{n}\right)^3\left(\frac{Q}{V_m}\right) \tag{3.7}$$

where λ_c/n is the fundamental cavity wavelength within the material, Q is the quality factor and V_m the mode volume of the cavity. In this equation the light emitter is on perfect resonance with the cavity and the dipole of the cavity mode completely overlaps with the dipole of the emitter. The linewidth of the emitter is neglected. Equation (3.7) is also known as Purcell's cavity figure of merit. Emission into leaky modes can be considered by inserting Q from equation (3.1).

3.2 Calculations

We calculated the Purcell factor for a micropillar with a 2 μm diameter from sample M4792 by using equation (3.7). The cavity resonance is located at 902 nm and the refractive index of the central GaAs layer at 5 K is assumed to be 3.4756 [19]. The optical pre-characterisation of this sample yields a quality factor of approximately 7900 , see figure 3.10. The volume of the cavity layer ($r^2\pi h = 0.767\,\mu\text{m}^3$) is in a first approximation assumed to be equal to the mode volume of the microresonator, which yields a Purcell factor of 13.4 . Therefore a quantum dot transition which is on resonance with the cavity should show a strong enhancement of the emission rate.

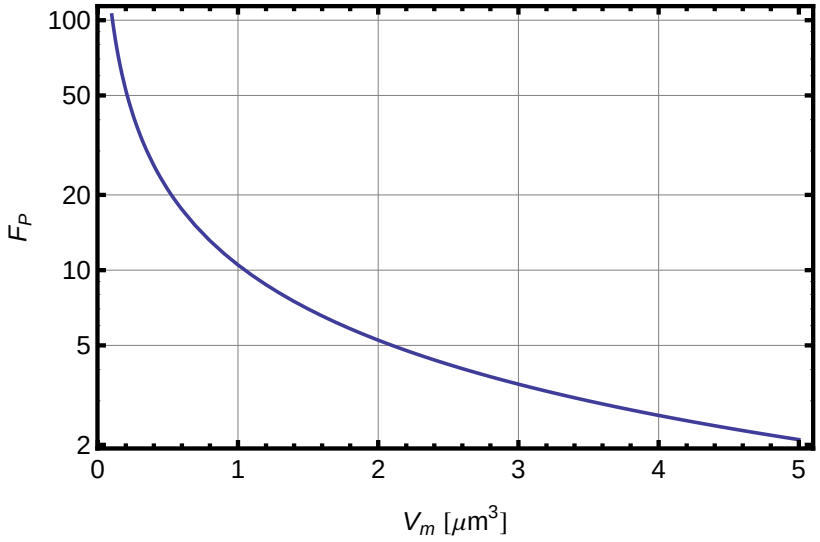

Figure 3.3: The Purcell factor as a function of the mode volume in μm^3. For this plot a GaAs microresonator with a resonance wavelength of 902 nm and a quality factor of 7900 is assumed. This value arises from the optical pre-characterisation of sample M4792, see figure 3.10.

For micropillar sample C3281 the same calculation yields a Purcell factor of 2.6 for a micropillar with a diameter of 2 μm. An experimentally obtained quality factor of 1500 , see figure 5.14 and a mode volume of 0.820 μm^3, see section 3.4.1 have been assumed.

3.3 Simulating Eigenmodes of Micropillars

In this section I would like to present a method for simulating the eigenmodes of micropillars [20, 29]. The notation for this formalism, follows reference [20]. Each layer of the micropillar is treated as an optical fibre with a radial step index profile. Figure 3.4 shows a schematic of a micropillar structure.

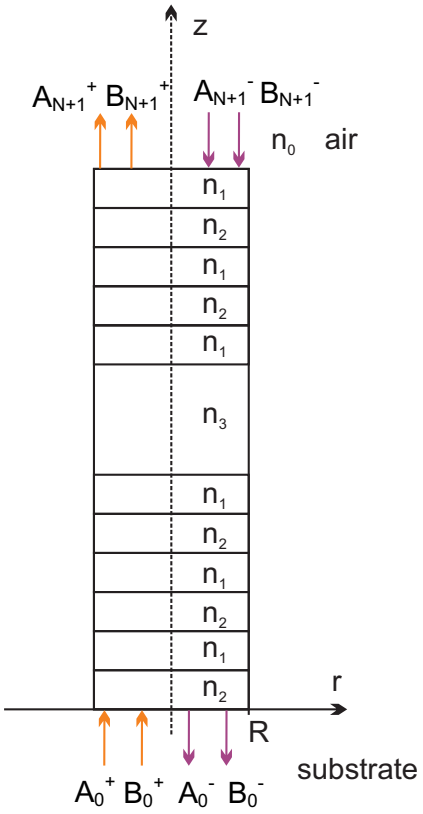

Figure 3.4: Profile of a micropillar. The DBR consists of alternating layers with refractive indices n_1 and n_2. The central layer has a refractive index of n_3. For $r > R$ and on top, air with n_0 is present. On the bottom the refractive index of the substrate is present. $A_l^{\pm}$ and $B_l^{\pm}$ are the amplitudes of forward and backward running waves at each layer l with TE_z and TM_z polarisation, respectively.

3.3.1 Solving Maxwell's Equations

The electric and magnetic field components are given by the solutions of Maxwell's equations inside and outside the micropillar with proper boundary conditions. The tangential field components have to be equal at the boundary ($r = R$) for forward and backward running waves [20]. These boundary conditions result in a transcendental equation which determines the eigenmodes of a cylindrical waveguide [29]:

$$\left(\frac{n^2}{\beta^2}\frac{\partial_r J_m}{J_m} + \frac{1}{\delta^2}\frac{\partial_r K_m}{K_m}\right)\left(\frac{1}{\beta^2}\frac{\partial_r J_m}{J_m} + \frac{1}{\delta^2}\frac{\partial_r K_m}{K_m}\right) = \frac{m^2 {k_z}^2}{R^2 {k_0}^2}\left(\frac{1}{\beta^2} + \frac{1}{\delta^2}\right)^2 \tag{3.8}$$

where

$$J_m = J_m(\beta R) \quad \text{and} \quad K_m = K_m(\delta R)$$

refer to the Bessel function of the first kind and the modified Bessel function of the first kind respectively. β is the transverse propagation constant inside the micropillar and δ describes the transverse attenuation constant on the outside.

$$\beta = \sqrt{k_0^2 n^2 - k_z^2} \tag{3.9}$$

$$\delta = \sqrt{k_z^2 - k_0^2} \tag{3.10}$$

R is the radius of the micropillar, n is the refractive index of the layer and $k_0 = \omega/c$ refers to the vacuum wavenumber. m describes the field variation in azimuthal direction. k_z refers to the longitudinal component of the wavevector and is the only unknown variable in (3.8). For practical reasons we express k_z as a function of β in equation (3.9) and solve β in the transcendental equation (3.8), by inserting a wavelength λ, a refractive index n and a radius R.

The two numbers m and l characterise the solution. The number l refers to the l^{th} smallest root[1] of the equation. m describes the order of the Bessel function and the modified Bessel function. In solutions with $m = 0$ the transcendental equation (3.8) separates into two independent equations. Here the solutions can be expressed as TE_z or TM_z eigenmodes [20]. For $m \geq 1$ both polarisations must be considered to satisfy the boundary conditions and therefore we obtain hybrid eigenmodes HE_{ml}.

3.3.2 Common Mode Approximation (CMA)

In general the longitudinal wavevector k_z has to be calculated from equation (3.8) for each layer of the micropillar. This is a very complex treatment of the system and would require intense numerical computation. Therefore we used the common mode approximation (CMA) in our simulations. The CMA is based on the assumption that the mode of the central layer is approximately the same in each DBR layer and that there is no coupling with other modes [20]. Furthermore within the CMA the TE_z and TM_z components of the hybrid mode are assumed to propagate separately and therefore each polarisation determines its own longitudinal mode.

In this approximation the transverse propagation constant β is calculated only in the central layer of the micropillar. Within the whole micropillar structure this value is assumed to remain unchanged. The longitudinal propagation constant γ_l of layer l, is defined by

[1] The smallest root is in the vicinity of he l^{th}-root of the Bessel function J_m.

$$\gamma_l = \sqrt{k_0^2 n_l^2 - \beta^2} \tag{3.11}$$

n_l refers to the refractive index of the l^{th} layer and $\gamma_l = k_z$ for the central layer.

The CMA is justified for low order modes and large micropillar radii. The approximation does not hold for high order modes and/or in the limit of $\lambda_R \approx R$ [20]. Here the diffraction losses in the cavity are dominant. The first condition is well fulfilled for our simulations. Due to the second condition we avoided simulating micropillars with radii smaller than $0.9\,\mu$m.

3.3.3 Transfer Matrix Method in CMA

This formalism offers a straightforward way to calculate the reflectivity for electromagnetic radiation for a certain wavelength in a distinct micropillar system (dimensions and refractive indices well known). The transmitted field amplitudes A_{N+1}^-, A_{N+1}^+, B_{N+1}^-, B_{N+1}^+ (see figure 3.4) are related to the incident field amplitudes A_0^-, A_0^+, B_0^-, B_0^+ with the transfer matrices M^{TE} and M^{TM} [20].

$$\begin{pmatrix} A_{N+1}^- \\ A_{N+1}^+ \end{pmatrix} = M^{\mathrm{TE}} \begin{pmatrix} A_0^- \\ A_0^+ \end{pmatrix} \tag{3.12}$$

$$\begin{pmatrix} B_{N+1}^- \\ B_{N+1}^+ \end{pmatrix} = M^{\mathrm{TM}} \begin{pmatrix} B_0^- \\ B_0^+ \end{pmatrix} \tag{3.13}$$

where

$$M^{\mathrm{TE}} = \prod_{l=0}^{N} M_l^{\mathrm{TE}} \quad \text{and} \quad M^{\mathrm{TM}} = \prod_{l=0}^{N} M_l^{\mathrm{TM}}$$

The final transfer matrices M^{TE} and M^{TM} are obtained by multiplication of the transfer matrices M_l^{TE} and M_l^{TM} of each layer l, respectively. These matrices are evaluated at every boundary[2] z_l and are defined by

$$M_l^{\mathrm{TE}} = \frac{1}{2} \begin{pmatrix} (1 + 1/\gamma_l^R)/e_l^- & (1 - 1/\gamma_l^R)/e_l^+ \\ (1 - 1/\gamma_l^R)e_l^+ & (1 + 1/\gamma_l^R)e_l^- \end{pmatrix} \tag{3.14}$$

$$M_l^{\mathrm{TM}} = \frac{1}{2} \begin{pmatrix} (\epsilon_l^R + \gamma_l^R)/e_l^- & (\epsilon_l^R - \gamma_l^R)/e_l^+ \\ (\epsilon_l^R - \gamma_l^R)e_l^+ & (\epsilon_l^R + \gamma_l^R)e_l^- \end{pmatrix} \tag{3.15}$$

where

$$\gamma_l^R \equiv \gamma_l/\gamma_{l+1}\ ,\ \epsilon_l^R \equiv (n_l/n_{l+1})^2 \text{ and } e_l^{\pm} \equiv \exp(i(\gamma_{l+1} \pm \gamma_l)z_l)$$

[2] In contrast to other transfer matrix method definitions [30] these matrices follow the definition of [31] Here z_l is the total length from the origin of the stack instead of a single layer thickness.

γ_l has to be evaluated numerically by the CMA (section 3.3.2).
Once the transfer matrix is obtained, the reflection coefficient for each polarisation can be calculated.

$$R^{\mathrm{TE}} = \frac{A_0^-}{A_0^+} = -\frac{M_{12}^{\mathrm{TE}}}{M_{11}^{\mathrm{TE}}} \mid_{A_{N+1}^-=0} \tag{3.16}$$

$$R^{\mathrm{TM}} = \frac{B_0^-}{B_0^+} = -\frac{M_{12}^{\mathrm{TM}}}{M_{11}^{\mathrm{TM}}} \mid_{B_{N+1}^-=0} \tag{3.17}$$

Since R^{TE} and R^{TM} have approximately the same values for low order modes and large micropillar radii [20], we can choose one polarisation for simulating the modal reflectivity.

3.4 Micropillar Samples with Quantum Dots embedded

3.4.1 Sample C3281

This sample was produced at the University of Würzburg. A low quantum dot density of approximately 10 to 20 dots per μm^2 should yield to a higher possibility of observing single quantum dots. The micropillar cavity mode is designed to be very close to the quantum dot's s-shell emission. This should yield to a higher spontaneous emission rate of the quantum dots due to the coupling with the cavity mode.

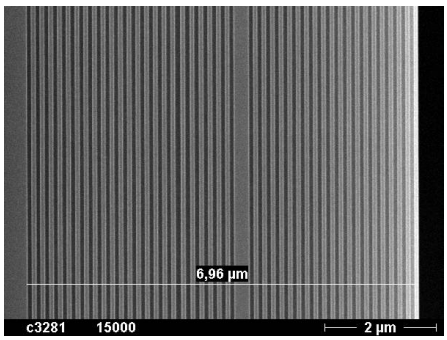

(a) The distributed Bragg reflector consists of 20 upper and 23.5 lower AlAs/GaAs mirror pairs.

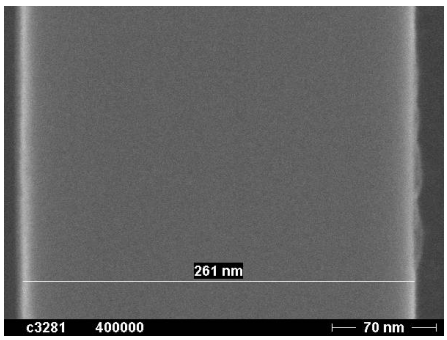

(b) The central cavity layer consists of GaAs and is 261 nm thick. The thickness of the AlAs/GaAs DBR layers is 80 nm and 69 nm, respectively.

Figure 3.5: Cleaved edge SEM images of sample C3281 before etching the micropilllars. (a) shows a profile of the sample. (b) is a zoom-in onto the central GaAs cavity layer. Pictures taken by [32].

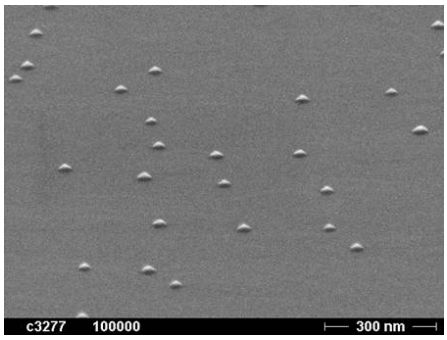

Figure 3.6: SEM image from [32] showing the quantum dots before overgrowing them with the upper cavity layers. A low quantum dot density of roughly 10 to 20 dots per μm^2 is present inside the center of the cavity.

An optical pre-characterisation of the sample was done by C. Schneider from University of Würzburg. The spectral reflectivity of the planar cavity at room temperature and before etching the micropillars and the emission spectrum of the InAs quantum dot ensemble at 20 K was measured, see figure 3.7. The fundamental resonance of the reflectivity spectrum (black line) is approximately at 975 nm at room temperature. Etching micropillars and lowering the temperature to 5 K blueshifts the cavity resonance. We expected the fundamental resonance to be at 928.5 nm, see figure 3.8. The s-shell of the quantum dots emits at about 930 nm and the wetting layer is visible at about 850 nm, see blue line in figure 3.7.

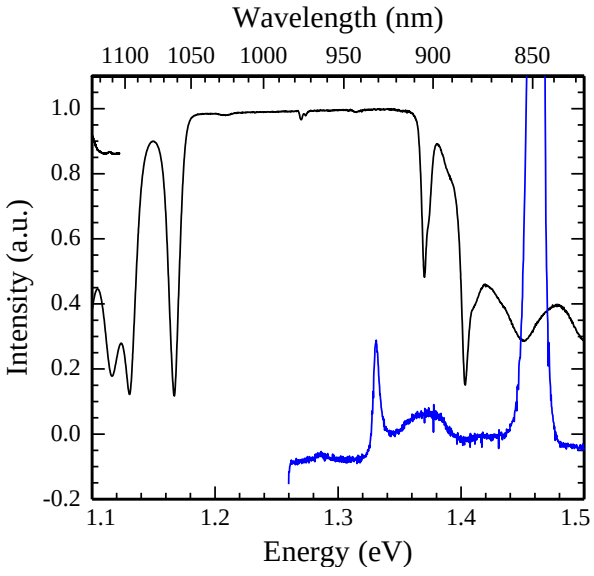

Figure 3.7: The black line shows the spectral reflectivity of the planar microcavity at room temperature. The blue line refers to the quantum dot emission and the emission from the wetting layer at 20 K. Image from [32].

We performed a simulation of the eigenmodes of micropillar sample C3281, see figures 3.8 and 3.9. For this we used refractive indices of 3.4756 for GaAs and 2.9205 for AlAs at 5 K [19]. The fundamental mode HE11 is at 928.3 nm. In section 5.2.5 we compare our simulation to the experimental observations.

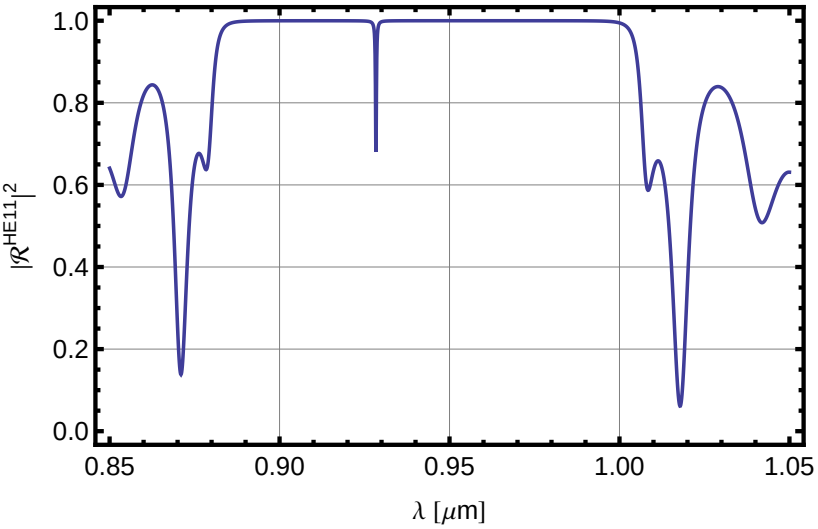

Figure 3.8: Simulated reflectivity spectrum for the HE11 eigenmode for a 1.8 μm diameter micropillar with 20/23.5 mirror pairs at 5 K. The layer thickness is 80 nm for AlAs, 69 nm for GaAs, and 261 nm for the central GaAs cavity layer [32]. For the simulation the method presented in section 3.3 was used.

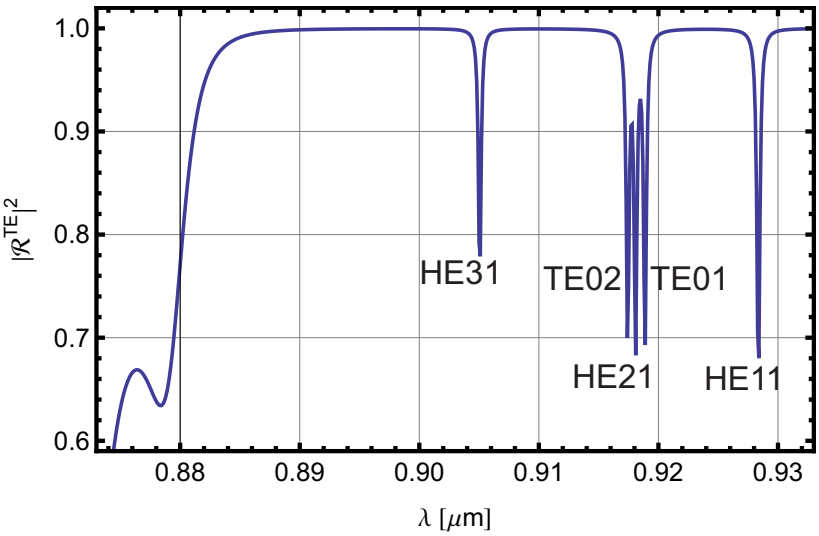

Figure 3.9: The simulated lowest order eigenmodes of a micropillar with the same properties as in figure 3.8.

3.4.2 Sample M4792

The samples M4792-4.1D and M4792-4.1B were produced by C. Schneider at the University of Würzburg. The samples both have the same properties regarding materials and dimensions. A 244 nm thick GaAs cavity layer is sandwiched between two AlAs/GaAs DBRs consisting of 20 upper mirror pairs and 30 lower mirror pairs, see figure 3.11. The micropillars were produced by using optical lithography. The quantum dot density is approximately 40 μm^{-2}. An optical pre-characterisation was done by C. Schneider. One result of this pre-characterisation is shown in figure 3.10. The fundamental resonance of a micropillar with a diameter of approximately 2 μm was measured at 902 nm.

In figure 3.12 the simulated lowest order eigenmodes of a 3 μm diameter micropillar with the properties of sample M4792 are shown. The mean mirror pair thickness was calculated from the total thickness of the DBR-reflectors and is 144 nm [32]. Therefore we assumed the layer thickness to be 65 nm for GaAs and 79 nm for AlAs. These values are bigger than the thicknesses in the detailed SEM image (see figure 3.11), but lead to a much better simulation. For the same reasons the cavitylayer is assumed to be thicker than in figure 3.11. We used the refractive indices of 3.4756 for GaAs and 2.9205 for AlAs at 5 K [19].

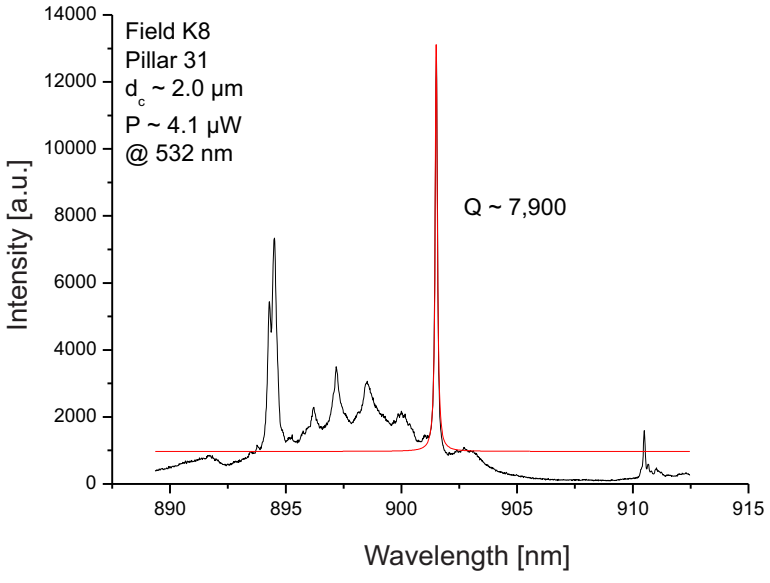

Figure 3.10: Photolumeniscence measurement of a ~2 μm diameter micropillar with above band excitation at 532 nm. The fit of the cavity resonance at 902 nm yields a quality factor of approximately 7900 . Image from [32].

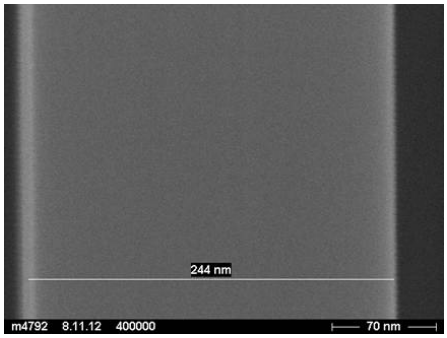

(a) The central cavity layer consists of GaAs and is approximately 244 nm thick.

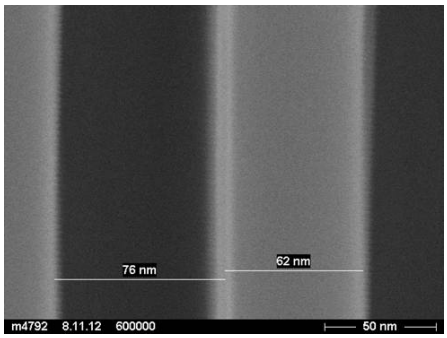

(b) The DBR consists of alternating GaAs/AlAs layers which have here a thickness of 62 nm and 76 nm respectively.

Figure 3.11: Cleaved edge SEM Images of the sample M4792 before etching the micropilllars from [32].

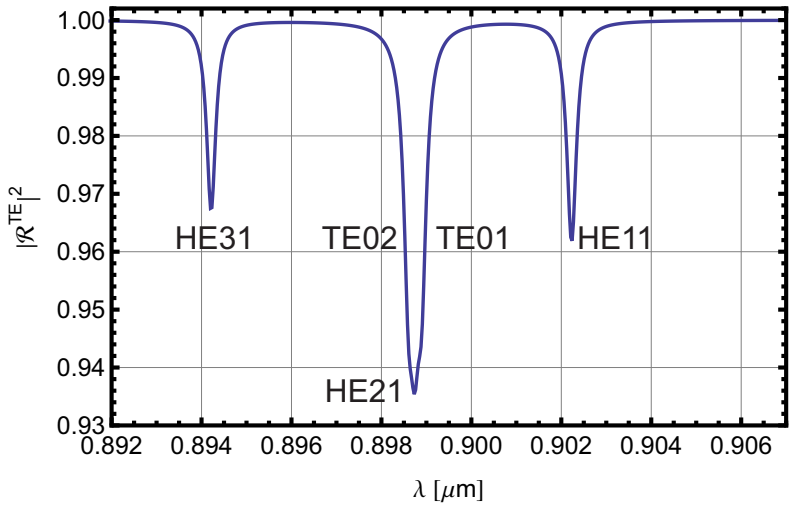

Figure 3.12: The simulated lowest order eigenmodes of a micropillar with a diameter of 3 μm with the properties of sample M4792 at 5 K. The layer thickness is assumed to be 79 nm for AlAs, 65 nm for GaAs and 253 nm for the central GaAs cavity layer [32]. For the simulation the method of section 3.3 was used.

Chapter 4

Photon Statistics

This chapter provides a short overview of the photon statistics of different light sources and introduce the second-order correlation function $g^{(2)}(\tau)$ [11]. The term photon statistics describes the temporal distribution of the emitted photons from one light source. There are three different classes of light regarding their photon statistics.

- Sub-Poissonian (antibunched photons) $\sigma < \sqrt{\overline{n}}$
- Poissonian (random photons) $\sigma = \sqrt{\overline{n}}$
- Super-Poissonian (bunched photons) $\sigma > \sqrt{\overline{n}}$

(a) bunched (b) random (c) antibunched

Figure 4.1: This pictures show the photon sequences of (a) bunched, (b) random and (c) antibunched photons.

In general one expects to find photons with super-Poissonian distribution with thermal light sources. Here the photons are bunched and it is more likely to detect photons with small time separation, see figure 4.1. A super-Poissonian distribution shows a standard deviation σ which is greater than the root of the expectation value ($\sigma > \sqrt{\overline{n}}$).
Coherent light, for example from a laser, which is operated well above the thresh-

old, shows a Poissonian photon statistics. This means that the detection of a photon has the same probability in every time interval of equal duration. We can say that the photons from such a light source are uncorrelated and therefore randomly distributed.
Nonclassical light is described by sub-Possonian photon statistics. A single photon source shows a sub-Possonian photon distribution. In general this means that the detected photons are antibunched. In a single quantum mechanical system, like an atom or a quantum dot, it is impossible that a second photon from the same transition is emitted before the system is reexcited. The total process takes a characteristic time which depends on the lifetime of the transition and the applied excitation power. Therefore single quantum mechanical systems produce antibunched photons.

4.1 The Second-Order Correlation Function $g^{(2)}(\tau)$

A method of describing the photon statistics of a light source consists of measuring the second-order correlation function. This function is proportional to the probability of detecting a second photon at time τ after the detection of a prior photon at time $\tau = 0$. The $g^{(2)}(\tau)$-function characterises the photon statistics of a light source [11] and is defined by

$$g^{(2)}(\tau) = \frac{\langle I(t)I(t+\tau)\rangle}{\langle I(t)\rangle^2} \tag{4.1}$$

$\langle I(t)\rangle$ refers to the averaged radiation intensity. Because the number of photons $n(t)$ is proportional to the intensity $I(t)$ of a light source, the second-order correlation function can be written as

$$g^{(2)}(\tau) = \frac{\langle n(t)n(t+\tau)\rangle}{\langle n(t)\rangle^2} \tag{4.2}$$

Some examples for the $g^{(2)}(\tau)$-function are plotted in figure 4.2. Strong photon antibunching $g^{(2)}(0) < 0.5$ is direct evidence that the radiation arises from a single photon emitter [11].

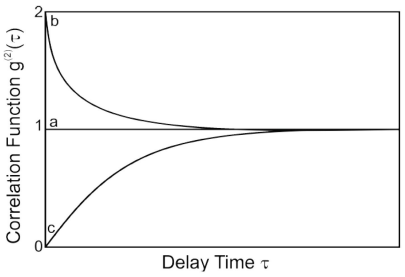

Figure 4.2: The $g^{(2)}(\tau)$-function for different emitters. (a) for an uncorrelated coherent emitter ($g^{(2)}(0) = 1$), (b) refers to super-Poissonian source ($1 < g^{(2)}(0) < 2$) and (c) to a single photon emitter (sub-Poissonian source with $g^{(2)}(0) = 0$). Image from [11].

4.2 Measuring Photon Statistics

Usually, the second-order correlation function is measured with the Hanbury-Brown-Twiss (HBT) setup [33]. A schematic of the HBT setup is shown in figure 4.3. A 50/50 beamsplitter directs the radiation onto two photodetectors. A detection at one photodetector starts a clock and the detection of a second photon at the other detector results in a stop. With the measured time intervals a histogram is produced. The histogram corresponds to the $g^{(2)}(\tau)$-function as long as the measured time intervals are much smaller than the mean time between two detection events [11].

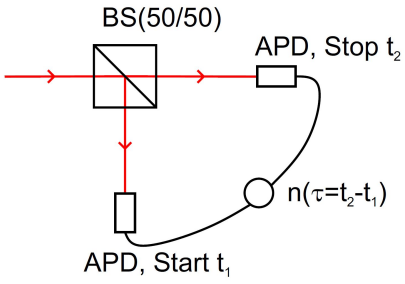

Figure 4.3: Schematic sketch of the Hanbury-Brown-Twiss setup for measuring photon statistics. A 50/50 beamsplitter (BS) directs the radiation to two different avalanche photo detectors (APDs). With the measured time difference between a detection event in one arm and the other a histogram is produced. Picture is taken from [34].

Chapter 5

Experiment

5.1 The Setup

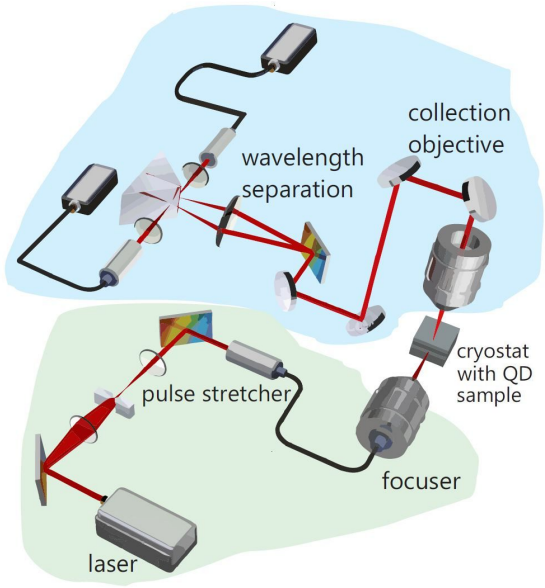

Figure 5.1: This picture shows the basic setup for side excitation and detecting the exciton- and biexciton emission. The blue shaded area is the analysing or collection part of the setup and the green shaded area is the excitation part. A detailed description of the setup can be found in the text.

The quantum dot sample is placed inside a continuous-flow liquid helium cryostat on top of a copper coldfinger in high vacuum (down to 0.05 mPa). A slight overpressure pushes liquid He out of a 250 l dewar and into the cryostat through

a vacuum insulated transfer line. A heat exchanger transfers the temperature to the coldfinger. The helium flow is adjustable with a valve and is approximately 1 l/hr. At the bottom of the coldfinger there is a temperature sensor. With an electrical heater and a PID-controller that controls a resistive heater the temperature can be varied and stabilized between 4.7 K and 60 K. Changing the temperature inside the cryostat always causes some movement of the sample position on the order of some micrometers. Through a top window and two side windows it is possible to optically excite and analyse the quantum dot emission. We always collect the photoluminescence through the top window with a high numerical aperture (0.70) objective. For monitoring the surface of the sample and determining the collection-position we use a red LED to illuminate the sample surface and a flip-mirror which directs the reflected light onto a CCD-camera. There are three different optical excitation techniques regarding their direction. The first one is called co-linear excitation, which means that the excitation path is also the analysing path. The excitation is therefore from the top. In our setup we use a pellicle beamsplitter with 90 % transmission to overlap the excitation path with the emission. Therefore most of the emitted photons can be collected in the analysing path and do not get reflected back into the excitation path. The simple setup for co-linear excitation is a big advantage because of the easy alignment. By making both paths exactly coincident one can very quick determine the exact position of a quantum dot on the sample. The disadvantage of this technique is the cavity stopband does not allow resonant excitation if the quantum dots are embedded into a distributed Bragg-reflector.
The second excitation technique is called side excitation. Here we use the waveguiding properties of planar cavity samples for which it is possible to couple photons from the side into the central layer. With this technique both resonant and above band excitation are possible. Almost no laser light scatters into the analysing path because of the orthogonal setup and the use of cross polarised excitation and emission. The disadvantage is that this kind of excitation is harder to align.
The third and last excitation technique which we use in our laboratory is called angle excitation. Here a focuser is placed under an angle to the horizontal direction as well as to the sample edge, see figure 5.2. Especially for micropillars which are positioned in the centre of the sample this seems to be the only possible optical excitation method which allows resonant excitation. The stopband would prevent a resonant excitation from top and the presence of other micropillars on the sample would not allow a side excitation of an inner micropillar.

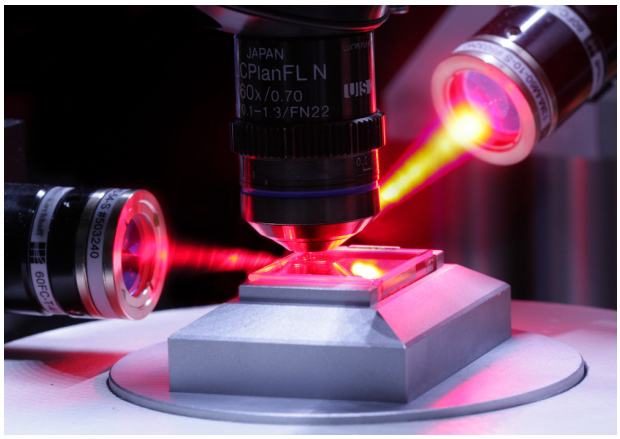

Figure 5.2: This picture shows the three different optical excitation techniques used in our setup: co-linear- (from top), side- and angle-excitation. A 60x microscope with a numerical aperture of 0.70 is used to collect the photo luminescence from the sample. The quantum dot samples are placed below the top window of the cryostat.

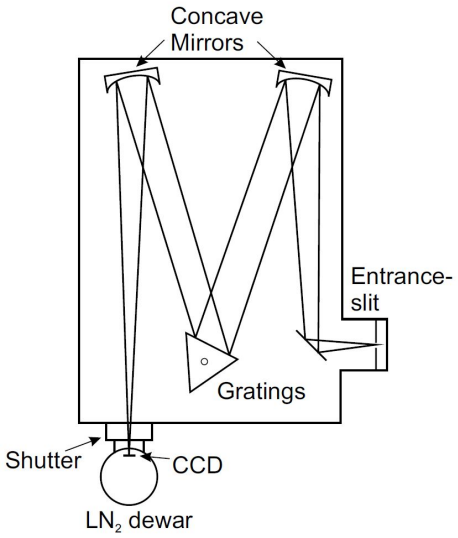

Figure 5.3: The spectrometer system consists of a grating monochromator and a liquid-nitrogen cooled CCD camera. Picture is taken from [15].

For above band excitation we use a simple diode laser at 636.16 nm. To perform resonant excitation a mode-locked Ti:Sapphire laser (Tsunami Model 3950 from Spectra-Physics) is used. The system is wavelength tunable from 690 nm to 1080 nm and also allows continuous wave (CW) operation. A repetition rate of 80 MHz and a tunable pulse length of 3 ps to 8 ps can be achieved with this system.

We use a pulse stretcher to be able to control the spectral width of the pulse. The pulse stretcher has a four-f-arrangement and consists of one grating and one slit. The grating is used twice. First the light gets diffracted onto the slit and then the spectrally filtered part is reassembled and exits the pulse stretcher. In figure 5.1 the old setup of the pulse stretcher with two gratings is drawn.
For spectroscopy measurements we use a spectrometer system which consists of a grating monochromator (Acton SP750i) and a liquid-nitrogen-cooled CCD camera (Princeton Instruments Spec-10 LN100BR). One can choose between three different gratings with 600, 1200 and 1500 rules per mm. Figure 5.3 shows a schematic drawing of our spectrometer system. The light is focussed on an entrance slit which cuts out most of the background light. After the first mirror the divergent beam is directed on a concave mirror which collimates the light and directs it onto the grating. A second concave mirror after the grating focuses the spectrally separated light onto the CCD camera. Alternatively, a second entrance and also a second exit can be used.
In addition to our spectrometer we built a second spectrometer specialized for collecting exciton- and biexciton emission at the same time. Here, we used a $1200\,\mathrm{mm}^{-1}$ grating (blazed for 900 nm) and two prism-mirrors to separate the exciton- and the biexciton emission. Both emission lines are then coupled into single mode fibres. Each fibre is connected to an avalanche photo diode (APD) (Single Photon Counting Module Array SPCM-AQ4C from Perkin Elmer). The home-made spectrometer is the end of the analysing path in our setup and allows a very fast access to correlation measurements, see figure 5.1. A 50/50 flip pellicle beamsplitter directs the light also into the normal spectrometer if needed.
The APDs at the end of the home-made spectrometer are connected to a multichannel event timer (HydraHarp 400 from Picoquant). A time resolution down to 1 ps can be achieved with the HydraHarp, but our APDs have a timing resolution of 250 ps only. For experiments which require a higher timing resolution we use APDs from Micro Photon Devices with a single photon timing resolution of 35 ps.

5.2 Spectroscopy

Spectroscopy is the measurement of radiation intensity as a function of wavelength or photon energy. In general, all spectroscopy measurements in our laboratory were performed with our spectrometer system (see figure 5.3). As described in section 5.1, above band excitation from top is the easiest way of observing the emission of a quantum dot sample.

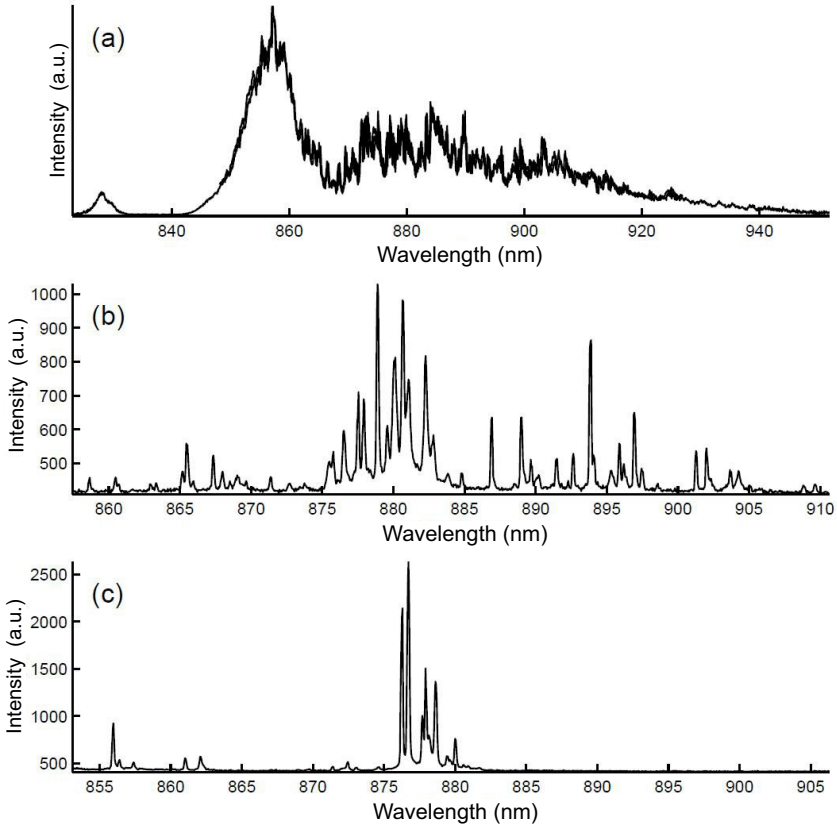

Figure 5.4: In [3] the emission under above band excitation from different area sizes of an InAs/GaAs quantum dot sample is shown. (a) shows the emission from an approximately 5 μm wide area, containing hundreds of quantum dots. In (b) the emission from a 0.8 μm wide area is displayed and in (c) an area with a diameter of 0.4 μm is investigated. (c) refers to a single quantum dot emission. Graphics adapted from [3].

Similar to the spectrum shown in figure 5.4 we have characterised the quantum dot density of the sample C3281-13,7 (section 2.4.2). One of the main aims of investigating this sample was to find the right aperture diameter with which a characterisation of single quantum dot states is possible. The top DBR of the sample was removed (only two mirror pairs left) and a mask was processed on top.

Holes with different diameters (from 0.2 μm to 4 μm) were etched into the mask which allows a diameter dependent observation of the quantum dot spectrum.

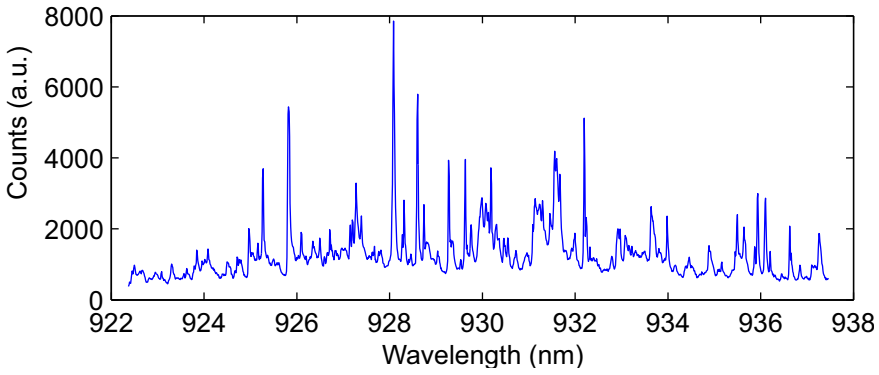

(a) 4 μm diameter

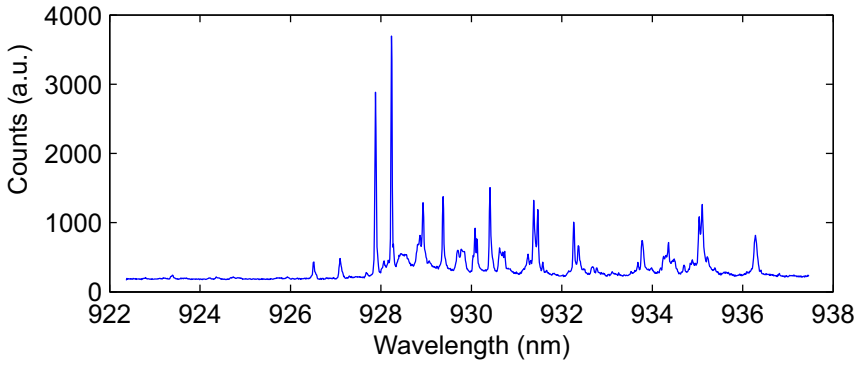

(b) 1 μm diameter

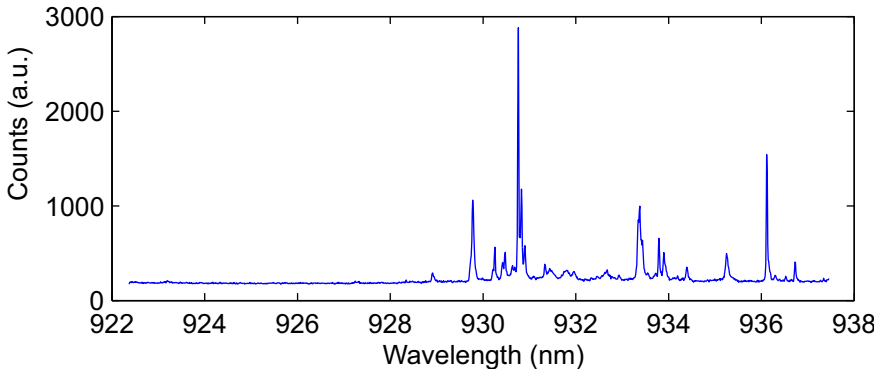

(c) 0.8 μm diameter

Figure 5.5: The emission of the quantum dots of sample C3281-13,7 with various aperture sizes. Above band excitation at 636 nm was used for excitation. As expected, the chance of observing single quantum dots increases with smaller aperture sizes. A diameter of 0.8 μm seemed most promising in terms of observing single quantum dots because smaller diameters often showed no emission.

5.2.1 Power-dependent Photoluminescence

Further characterisation of quantum dot states requires power-dependent photoluminescence measurements. These measurements offer a straight forward method to distinguish between the emission from multi-particle states and single-particle states in quantum dots.

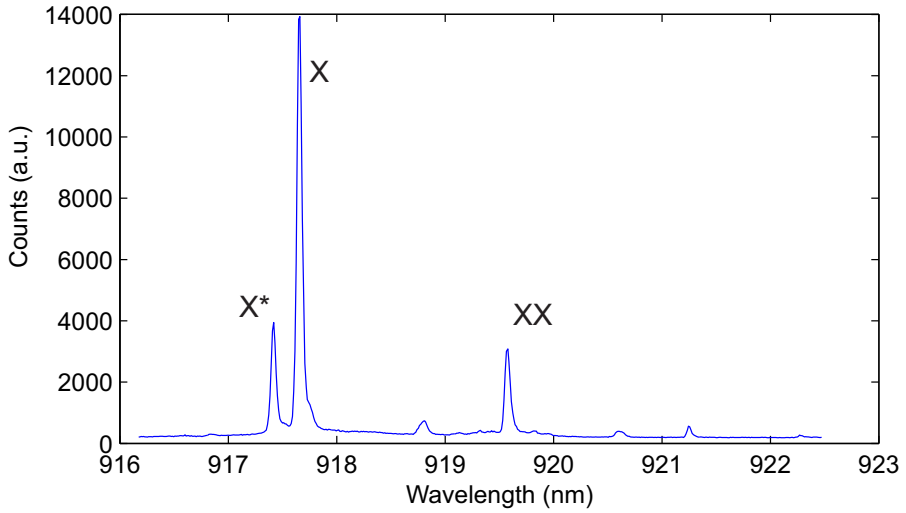

Figure 5.6: The emission spectrum of *dot5b* at sample #m649 under above band excitation with 636.16 nm. We measured the power-dependence of two emission lines (X at 917.65 nm and XX at 919.58 nm) and plotted the results in figure 5.7.

By increasing the excitation power it is possible to characterize multi-particle states within the quantum dot. The chances to generate a biexciton state are mainly dependent on the occupation of the exciton state and the presence of additional free charge carriers. Since the occupation of the exciton state is itself linearly dependent on the number of free charge carriers in the surrounding, which is proportional to the number of absorbed photons, the biexciton- and the exciton-intensity have a different dependence on the laser power. With this simple model one can assume that the exciton is linearly dependent on the input laser power and that the biexciton shows a quadratic power dependence.
The third line in figure 5.7 shows almost quadratic power-dependence and therefore this emission line should refer to a four-particle state, a biexciton. The exponents of 0.99 and 1.95 are both slightly smaller than expected within this model. This mismatch can be explained by other nonlinear power-dependent recombination processes which are not observed within this measurement.

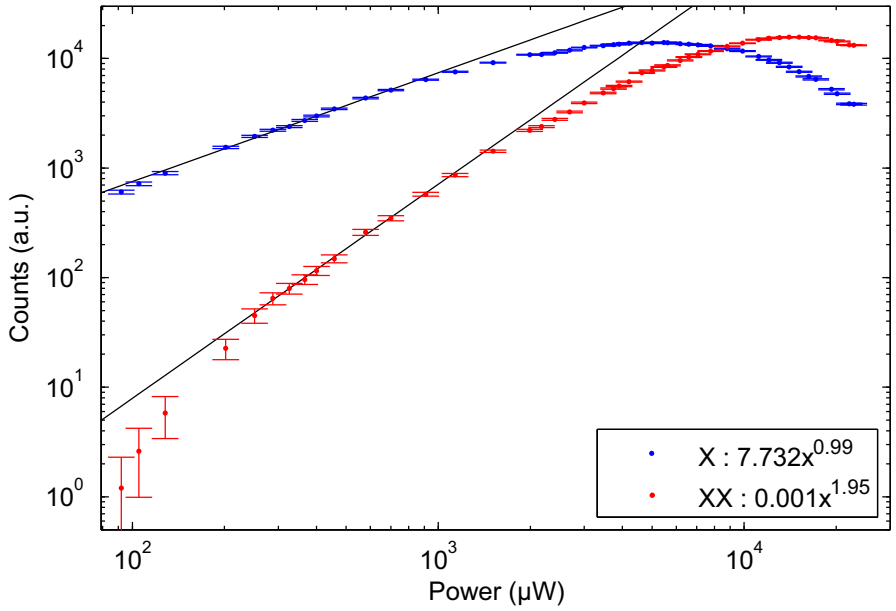

Figure 5.7: The intensity of the emission lines X and XX from *dot5b* on sample #m649 (see figure 5.6) as a function of excitation power in a log-log plot. A wavelength specific background correction is applied. For the fitting we considered only the linear part in this logarithmic plot, before saturation effects occur.

On calibration sample C3281-13,7 we did some statistics on power-dependent photoluminescence measurements. The aim was to get an idea of the percentage of quantum dots which show biexcitonic emission. We measured the power-dependence of 38 emission lines from areas with smaller diameters than 1.25 μm. Larger diameters showed simply too many emission lines to guarantee a successful measurement. Only three emission lines with quadratic power-dependence were observed. Therefore, the ratio of biexcitonic to excitonic emission is approximately 10 % which is very low compared to sample #m649, in which a ratio of approximately 60 % was found. The growth process of self-assembled InAs quantum dots has major influence on the biexciton-exciton ratio and therefore these statistics are an important feedback for the future growth of samples.

5.2.2 Temperature-dependent Photoluminescence

To control the influence of the Purcell effect on the quantum dot emission, one of the first things we investigated is the temperature tunability. In general, the cavity and the quantum dot emission wavelength have a different temperature dependence. Observing the spectrum and changing the sample temperature should show the enhancement of the quantum dot emission whenever a line gets into resonance with the cavity.

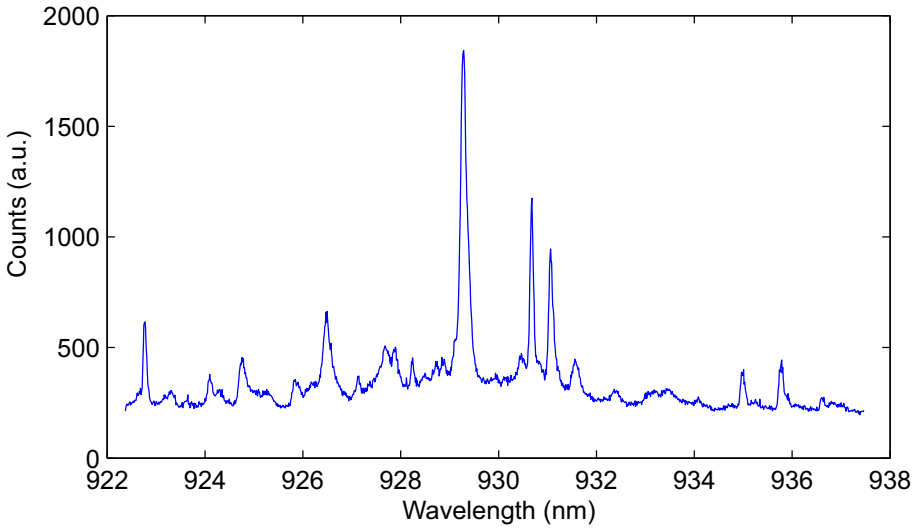

Figure 5.8: Spectrum from a micropillar from sample C3281 with a diameter of 1.8 μm. This micropillar is located at the first row and column number nine of the sample (micropillar 1.8 μm 1-9). For excitation we used a pulsed Ti:Sapphire laser at 854 nm.

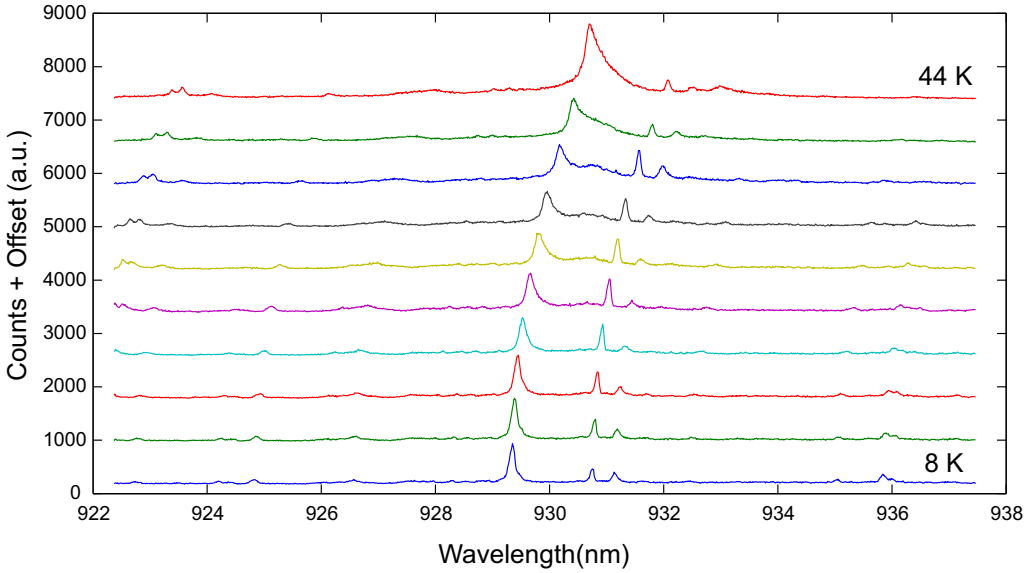

Figure 5.9: Emission from the same micropillar 1.8 μm 1-9 for temperatures from 8 K to 44 K. Each 4 K a spectrum was taken. The first line shows an enhancement of the signal when the emission is at approximately 930.5 nm. The emission-intensity of the second bright emission line seems to get enhanced between 12 K and 28 K.

The temperature dependence of the emission from micropillar 1.8 μm 1-9 gives a first impression of the quantum dot-cavity-coupling. In order to further characterise the emission lines from figure 5.8 and the strength of the coupling we performed correlation measurements and lifetime measurements. These measurements will be discussed in the next sections.

5.2.3 Time-Resolved Spectroscopy

For measuring the lifetime of excited states of quantum dots we used time-resolved spectroscopy, which means that we measured the arrival of emitted photons with respect to the excitation pulse. To maximize the temporal resolution we used APDs from Micro Photon Devices (Timing resolution: 35 ps). When observing light from a single quantum dot transition one expects an exponential decay of the signal with time after the excitation process is turned off. The lifetime is shortened when its emission is on resonance with the cavity and therefore the measurement of the lifetime is a method to observe the Purcell effect. To show the principle of time-resolved spectroscopy we measured the lifetime of a bright emission line at 930 nm from a 1.6 μm diameter micropillar in row 20 column 8 on sample C3281 and fitted an exponential decay to the data, see figure 5.10.

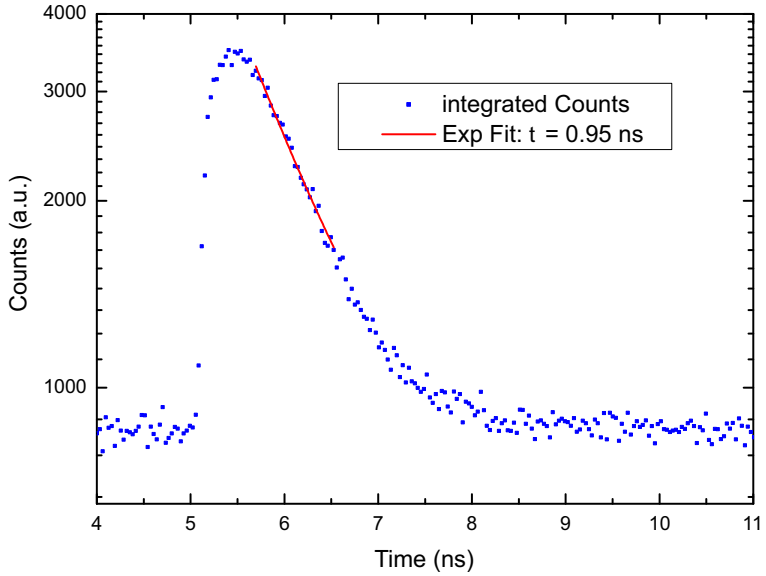

Figure 5.10: A logarithmic plot of the emission arrival of the bright line of a 1.6 μm diameter micropillar 20-8 on sample C3281. The quantum dot was excited with a pulsed Ti:Sapphire laser at 800 nm and a power of 60 μW. The exponential fit yields a lifetime of 0.95 $\pm$ 0.19 ns.

Compared to other excitons the lifetime in figure 5.10 is not shorter and therefore no influence from the cavity is expected to be present. Furthermore,

by detuning the emission with temperature, the lifetime of the state stays almost constant which also indicates that the quantum dot does not couple to the cavity.

To characterise the influence of the Purcell effect we studied the emission lines of micropillar 1.8 μm 1-9 (see figure 5.8) and measured their lifetimes at different temperatures. Especially the second bright line showed an interesting change of its lifetime.

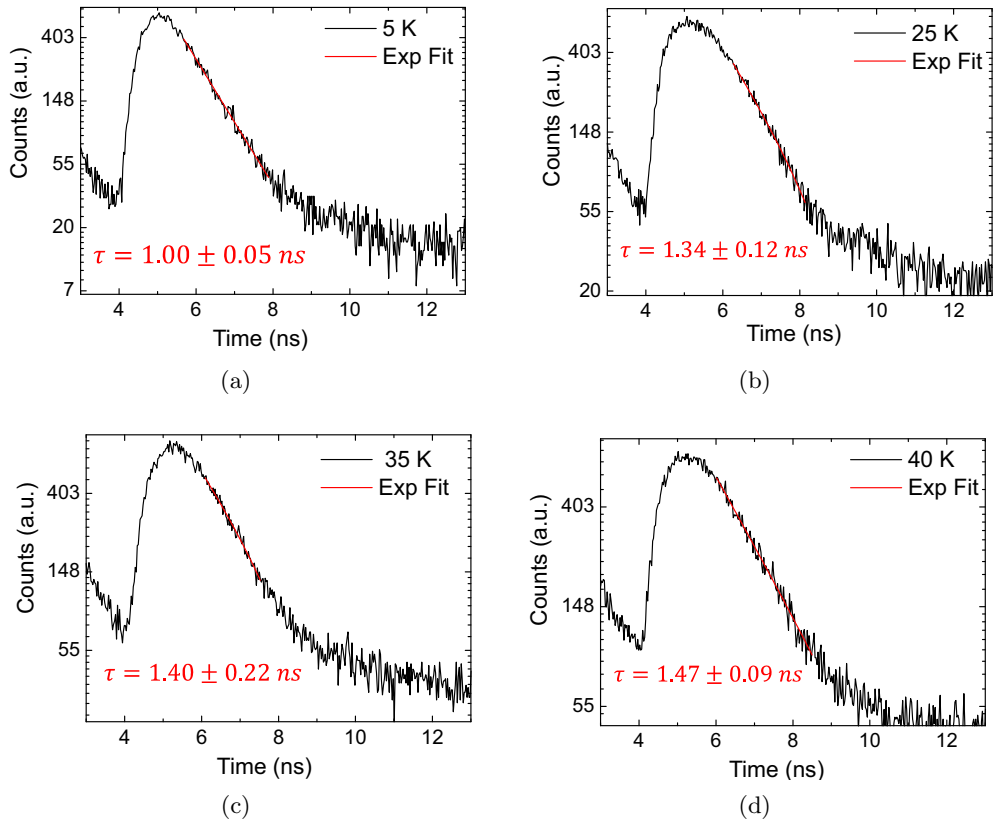

Figure 5.11: The lifetime of the second bright line of micropillar 1.8 μm 1-9 (see figure 5.8) at different temperatures. (a) refers to 5 K, (b) to 25 K, (c) to 35 K and (d) to 40 K. This line shows a coupling to the cavity at low temperatures. By detuning the emission from the resonance by temperature the lifetime of the state gets longer by a factor of 1.5. Exact values for the lifetime are 1.00 ± 0.05 ns at 5 K, 1.34 ± 0.12 ns at 25 K, 1.40 ± 0.22 ns at 35 K and 1.47 ± 0.09 ns at 40 K.

5.2.4 Measuring the Spectral Reflectivity

We performed a measurement of the spectral reflectivity of sample #m649. Previously the reflectivity of the planar cavity structure was simulated by using the transfer matrix method from [18]. The results are plotted in figure 5.12 and in figure 5.13.

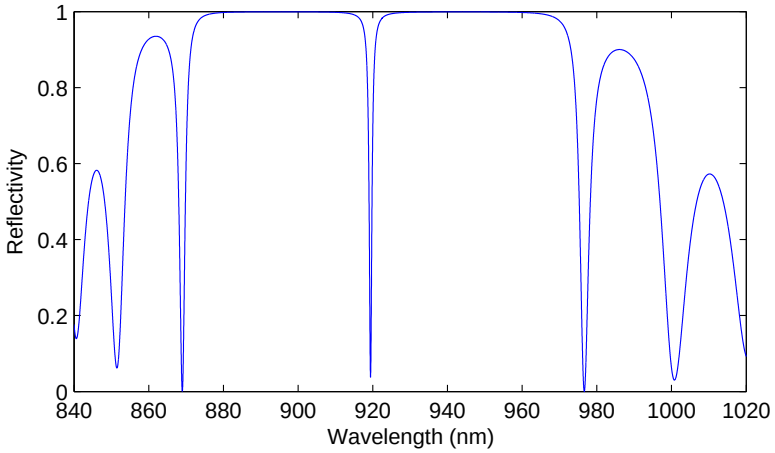

Figure 5.12: Theoretical reflectivity spectrum for TE-polarized light with normal incidence for a four-λ-cavity with a DBR consisting of 10 upper and 16 lower mirror pairs at 10 K. The cavity resonance is at 919.4 nm. For the calculation the refractive indices of GaAs and AlAs in [19] were used. The stopband of the system reaches from 869 nm to 977 nm. The code for this transfer matrix calculation was implemented by G. Weihs.

For the measurement we illuminated the sample with a white light source (CMS Schreder type WLS 100). The reflectivity spectrum was measured with our spectrometer system with the 600 rules per mm grating. The fundamental mode of the cavity is at 919.4 nm (see figure 5.13). The efficiency of our setup and the intensity of the white light source is wavelength dependent which leads to an intensity decrease at both sides of the originally measured reflectivity spectrum. Furthermore, the alignment efficiency of the used spectrometer system was maximal for the center of the observed wavelength range. Figure 5.13 shows the normalised reflectivity spectrum and consists in total of five measured spectra. Therefore, we observe local broad maxima every 50 nm.

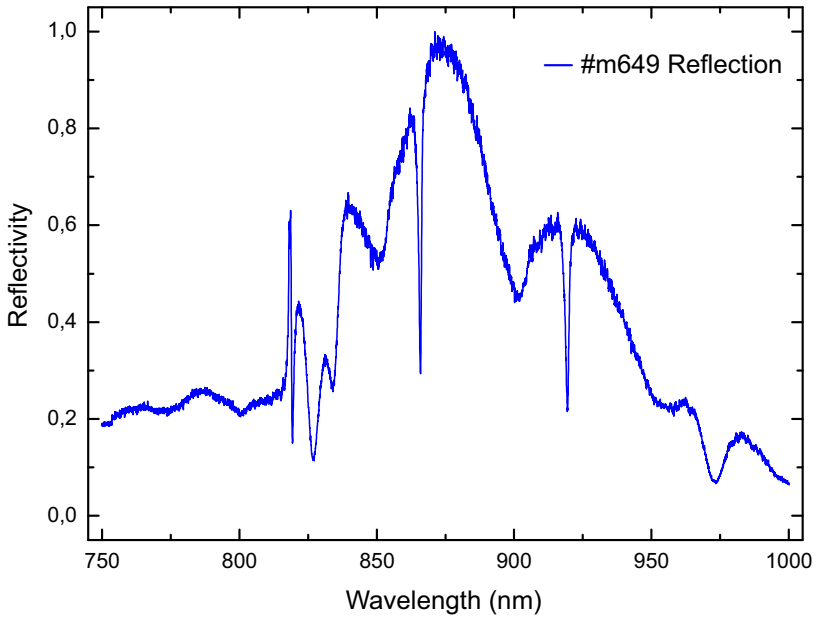

Figure 5.13: The normalised reflectivity spectrum of sample #m649. The resonance of the cavity is at 919.4 nm. Because of the simulation we expect the dips in the measured spectrum at 866 nm and at 974 nm to mark the boundaries of the stop band.

5.2.5 Spectroscopy of the Fundamental Micropillar Eigenmode

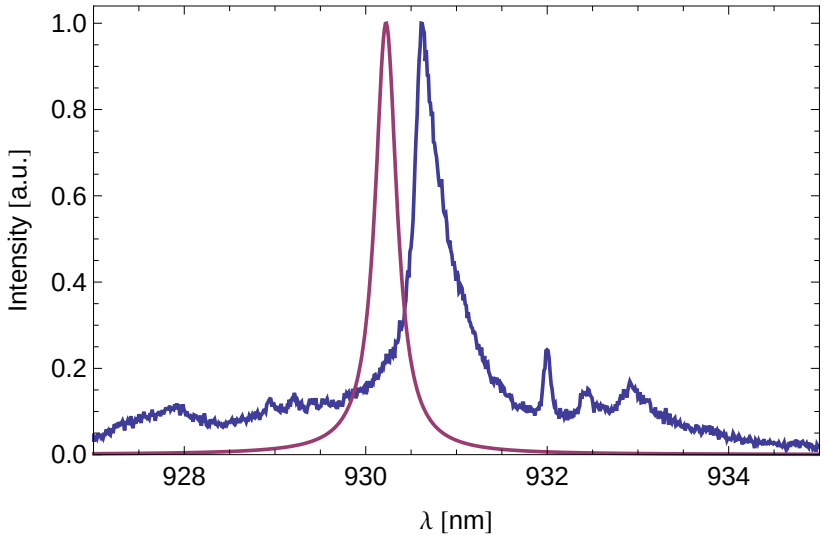

Figure 5.14: Measured and simulated spectral transmittance for the micropillar 1.8 μm 1-9 at 44 K, see figure 5.8. For comparison reasons the maximal intensity of the simulation and the measurement are set to one.

We measured the spectral distribution of the fundamental HE11 eigenmode for a 1.8 μm diameter micropillar 1-9 from sample C3281 at 44 K (figure 5.8). We used above band excitation to be able to observe the fundamental eigenmode of the micropillar. For the simulation the refractive indices of 2.9264 for AlAs and 3.4831 for GaAs were used [19]. An exact knowledge of the refractive indices of the two different materials is very important for a successful simulation. Changing the refractive indices only 0.1 % shifts the HE11 eigenmode in figure 5.14 by 1 nm. Therefore we can say that the result of this measurement is in good agreement with the eigenmode simulation result.

5.3 Correlation Measurements

With these measurements the photon statistics of the light source can be characterised. Furthermore, with cross-correlation measurements it is possible to observe and characterise cascade emission in a quantum dot. In general a temporal photon correlation measurement describes the probability of a light source for emitting a photon at time t_2 if a photon at time t_1 was emitted. To measure the signal of a single quantum dot all sources of background light have to be removed. Due to the low photon rate (at the moment maximally 400k photons per second from the biexciton emission with resonant two photon excitation, collected in a single mode fibre) very sensitive single photon detectors are needed. We used the Single Photon Counting Module Array from Perkin Elmer with a timing resolution of 250 ps and a photon detection efficiency of approximately 20 % for 930 nm. The detector dead time of 50 ns is irrelevant for our experiments because we are always using two different detectors for measuring photon-correlations.

For our correlation measurements we measured the second-order correlation function ($g^{(2)}(\tau)$), see chapter 4. Two different classes of correlation measurements were performed:

- Auto-correlation: Photons from one emission line.
- Cross-correlation: Photons from two different emission lines.

5.3.1 Auto-Correlation Measurement

As described in chapter 4, with a measurement of the second-order correlation function one can experimentally verify that quantum dots are single photon emitters. We performed an auto-correlation measurement for the second bright line of micropillar 1.8 μm 1-9. The result is plotted in figure 5.15. Due to the darkcount-level of 400 Counts per second on our APDs and the present small probability of

multi-photon emission we do not expect the $g^{(2)}(\tau)$-function to reach zero. The normalized $g^{(2)}(\tau)$-function was fitted with $1 - ae^{|\tau/b-c|}$. For very low excitation power the denominator in the exponent b corresponds to the lifetime of the state, [35]. Here, we used an excitation power of 1 μW and by comparing this value with the measured lifetime in section 5.2.3 we can see that the value is smaller by a factor of 1.41 . The measured value is artificially shortened by the high pumprate of the laser.

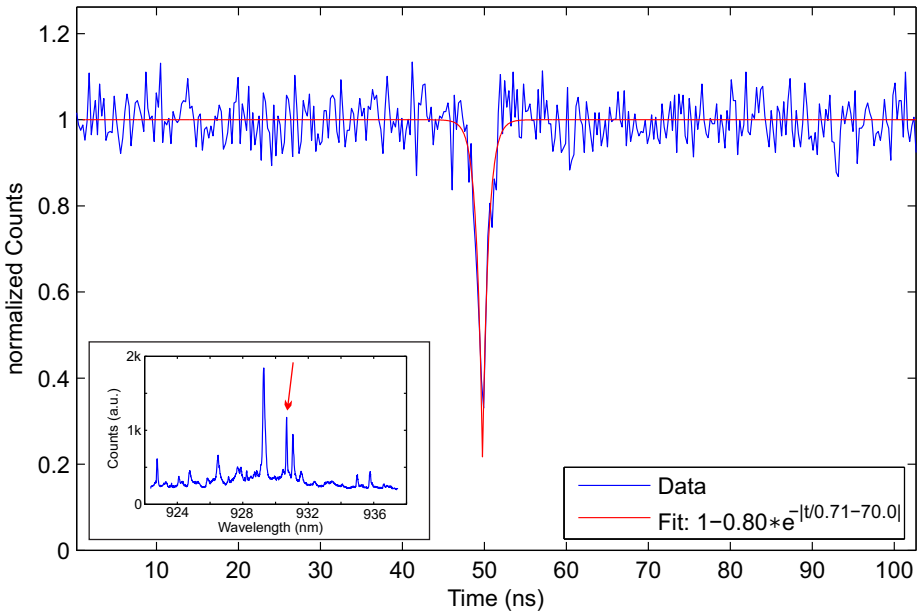

Figure 5.15: Result for an auto-correlation measurement of the second line of micropillar 1.8 μm 1-9. The inset shows the spectrum of this micropillar. The dip of the $g^{(2)}$-function indicates the single photon character of the emission line. The measurement was taken at 5 K exciting above band with a continuous wave diode-laser with 1 μW power.

Besides the continuous wave excitation, an auto-correlation measurement can also be performed with pulsed excitation. Due to the pulse length of only a few picoseconds the quantum dot state does not get reexcited within one pulse. Therefore, for a perfect single photon source one expects the central peak to be missing. In general, a central peak area of $g^{(2)}(0) < 0.5$ indicates light from a single quantum emitter [11]. For normalisation one can normalize the histogram by the corresponding values of a Poissonian distributed light source with equal radiation intensity.
We performed a pulsed auto-correlation measurement for *dot5b* on sample #m649. The result is plotted in figure 5.17. For excitation we used the two-photon excitation method, which is discussed in section 2.2.2, with a mode-locked Ti:Sapphire laser (repetition rate of 80 MHz). This method resonantly populates the biexci-

ton state of the quantum dot. The spectrum is shown in figure 5.16. The central broad peak originates from excitation laser scattering. The other sharp emission lines belong to the exciton (X), the biexciton (XX) and the trion (X*) state.

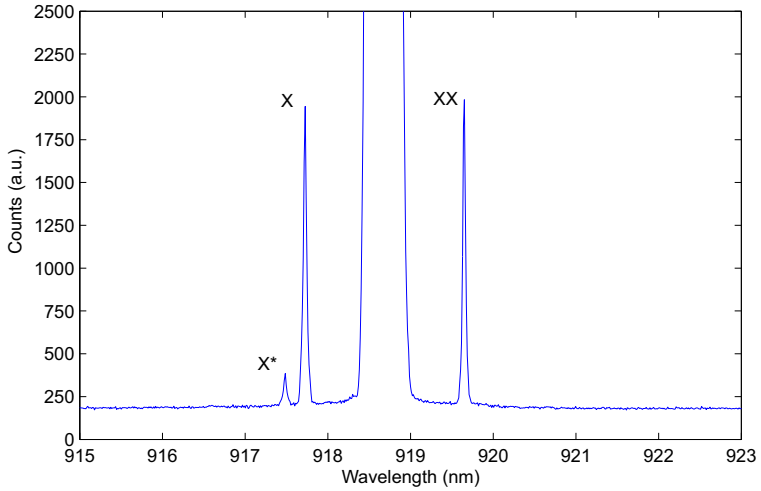

Figure 5.16: Photoluminescence from *dot5b* at sample #469 with resonant two photon excitation. The central broad peak corresponds to scattering from the excitation laser. The states of this quantum dot are labelled as follows: exciton (X), biexciton (XX) and trion (X*).

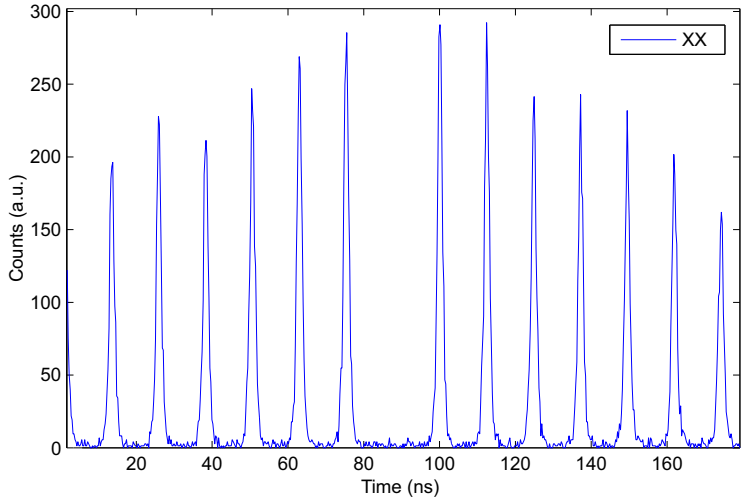

Figure 5.17: Auto-correlation measurement of biexciton photons of *dot5b* with pulsed two photon excitation. The missing central peak indicates the strong suppression of two photon events. The decrease in height of the side peaks is due to blinking [3].

5.3.2 Cross-Correlation Measurement

For characterizing quantum dot states we can use cross-correlation measurements. Figure 5.1 provides an overview of the basic setup of this measurement. Here, photons of two different emission lines are collected separately and correlations between the two emission lines are measured. Again, a photon detection in one arm starts a timer and a detection in the other arm stops the timer. The measured time intervals are plotted in a histogram. For a low photon flux and for measured time separations shorter than the mean time between detection events, this histogram is proportional to the second-order cross-correlation function:

$$g^{(2)}_{i,j}(\tau) = \frac{\langle I_i(t) I_j(t+\tau)\rangle}{\langle I_i(t)\rangle \langle I_j(t)\rangle} \tag{5.1}$$

where $I_j(t)$ is the measured intensity of the j^{th} transition. The second-order cross-correlation function $g^{(2)}_{i,j}(\tau)$ describes the probability of detecting a photon from transition i at time τ, if a photon from transition j is detected at time $\tau = 0$.

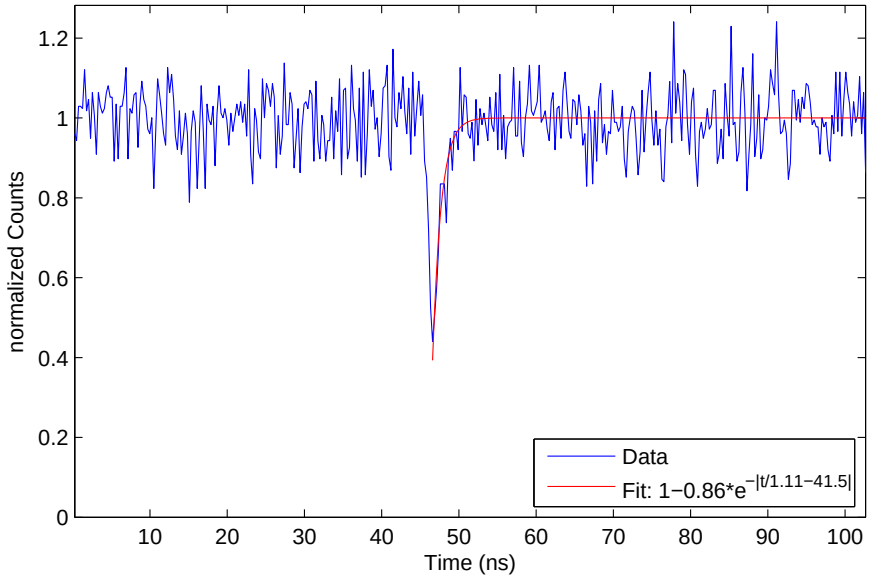

Figure 5.18: Cross-correlation measurement of the second line and the third line from micropillar 1.8 μm 1-9 in figure 5.8. The dip of the cross-correlation function indicates that both emission lines origin from the same emitter. The asymmetry indicates that one of the emission lines is a trion, see text. This measurement was taken at 5 K with a continuous wave diode-laser with 0.92 μW power.

In figure 5.18 a cross-correlation measurement between an exciton and a trion is shown. The antibunching indicates once again that those two emission lines originate from the same quantum dot. The asymmetry of the dip can be explained by one emission line belonging to a trion [11, 36]. After recombination of the trion the quantum dot is singly charged. Injecting another single charge carrier into the quantum dot takes considerably less time than to inject a triple charge after the emission of an exciton. In the limit of very high excitation power of the laser (the pumprate is much bigger than the recombination rate) the denominator of the exponent in the fit of figure 5.18 (1.11 ns) would correspond to the triple charge injection load time. However, with an excitation power of 0.92 μW we are not expecting to be in this limit and therefore this value can not be directly assigned to the lifetime nor to the load time of the trion.

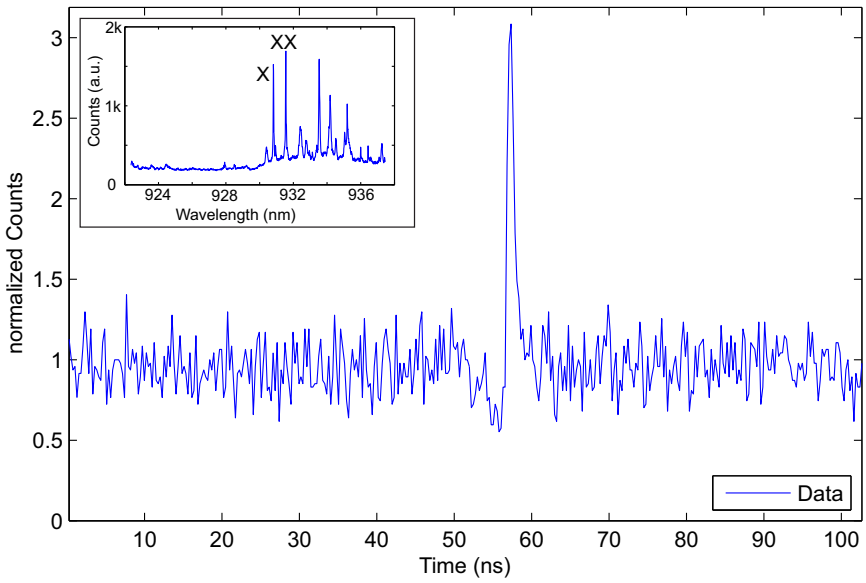

Figure 5.19: Cross-correlation measurement of an exciton (X) and a biexciton (XX) state of area K4 2/4 on sample C3281-13,7. The inset shows the spectrum of this area with above band excitation. The peak right next to the center of the $g^{(2)}$-function indicates that one emission is always right after the other one. This behaviour can be explained by the fact that one emission line corresponds to an biexciton and the other to an exciton.

We performed a cross-correlation measurement of a biexciton- and an exciton emission of area K4 2/4 at sample C3281-13,7, see inset of figure 5.19. The result is plotted in figure 5.19. After the emission of a biexciton photon the quantum dot is in the exciton state. Therefore, we have a high probability to measure an exciton photon right after the arrival of a biexciton photon. This high probability yields a peak after the zero-point of the $g^{(2)}$-function, if the biexciton

photon arrives before the exciton photon and starts the measurement. On the other hand, if the exciton photon detection starts the timer, then the peak would be before the zero-point of the $g^{(2)}$-function. The dip before the zero-point of the $g^{(2)}$-function in figure 5.19 occurs because, after the detection of an exciton photon the quantum dot is empty and it takes a characteristic time to fill the quantum dot again with two electrons and two holes before the next biexciton photon can be emitted and afterwards detected.

5.4 Two-Photon Interference

In 1987 C. K. Hong, Z. Y. Ou and L. Mandel published the effect of two-photon interference of photons generated with parametric down-conversion process [37]. This is one effect that unambiguously demonstrates the quantized nature of the electromagnetic field..

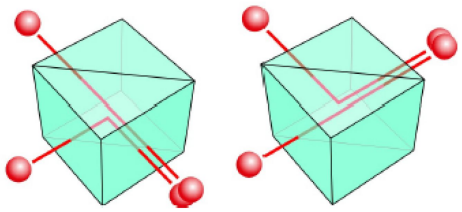

Figure 5.20: Schematic of two-photon interference. Two indistinguishable photons entering a beamsplitter at the same time from different inputs always leave the beamsplitter together. Picture is taken from [38].

If two indistinguishable photons enter a beamsplitter at the same time from different inputs, there is a 50/50 probability for them to leave both either at the first or at the second output. The case that one photon is transmitted and one is reflected is ruled out by quantum theory and only possible if the incident photons are distinguishable [37], which means that they do not enter the beamsplitter at the same time for example. By changing the arrival time difference of the photons (usually by changing the path length of one input arm) and detecting coincidence events of the beamsplitter outputs, one can measure the Hong-Ou-Mandel dip: A high degree of indistinguishability yields total absence of any coincidence counts if the arrival time difference is zero. Figure 5.21 shows the originally observed two-photon interference by Hong-Ou-Mandel [37]. The width of the Hong-Ou-Mandel dip corresponds to the coherence length of the wavepackets [39].

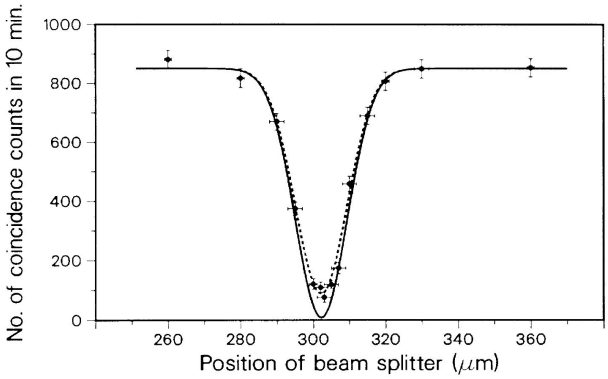

Figure 5.21: Plot of the coincidence counts in 10 min against the position of the beamsplitter. The position of the beamsplitter is proportional to the difference of the photon arrival times. Image taken from [37].

We performed a two-photon interference measurement using a resonantly excited InAs quantum dot. We used pulsed p-shell excitation for populating the exciton level of *dot5b* from sample #m649. Figure 5.22 shows the experimental setup for this measurement.

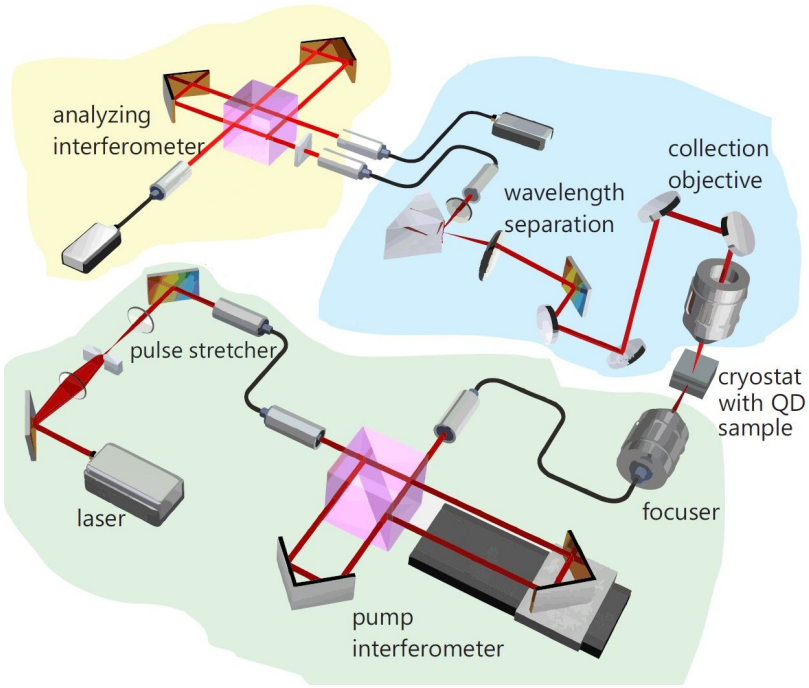

Figure 5.22: Experimental setup for measuring two-photon interference from a quantum dot. The three major parts of this setup are the excitation path with the pump interferometer (green), the collection path (blue) and the analysing interferometer (yellow). Further description is in the text.

The pulses from the excitation laser with a repetition rate of 80 MHz pass a Michelson interferometer, in which the length of one arm can be varied. This results in a change of the time delay between two successive excitations. The exciton emission is collected and the two emission pulses enter one input of the analysing interferometer. Therefore, at the two outputs of the interferometer each detector observes three pulses in which the intensity of the middle pulse is twice as high as the other two pulses (1:2:1). For the measurement of the coincidences each of the three pulses can start the timer and each of the three pulses from the other output of the interferometer can stop the timer. By considering each combination and its relative intensity one expects to measure a five-peak cluster with a relative intensity variation of 1:4:6:4:1. This pulse cluster repeats itself every 12.5 ns because of the repetition rate of the laser.
For nonclassical light with perfect two-photon-interference one expects the intensity ratio of the central five-peak-cluster to be at 1:2:0:2:1 [3]. It is obvious that the central peak at $\tau = 0$ has to disappear, if the emitted photons arrive at the same time on the beamsplitter. For the ratio of the two side peaks one has to take into account the other combinations that occur in the case of perfect two-photon interference.
In figure 5.23 the case of nonclassical light with perfect two-photon interference and the case of classical light pulses with no interference are compared.

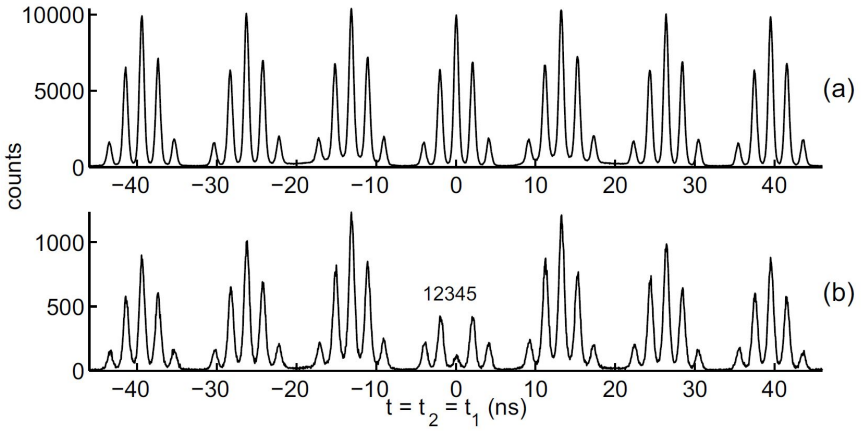

Figure 5.23: Theoretical expectation for photon correlations obtained from the experimental setup in figure 5.22. The origin of the five-peak clusters is described in the text. (a) for scattered laser pulses and (b) for a single photon source with two-photon-interference. Picture is taken from [3].

To show the Hong-Ou-Mandel dip of the exciton emission we normalised the measured intensity of the central peak to the intensity of the mean value by peak two and four in figure 5.23. This value was plotted against the photon arrival

time difference, see figure 5.24. We used a pulsed Ti:Sapphire laser at 879.22 nm with a power of 161 μW for excitation. The quantum dot was excited from the side and had a sample temperature of 4.8 K.

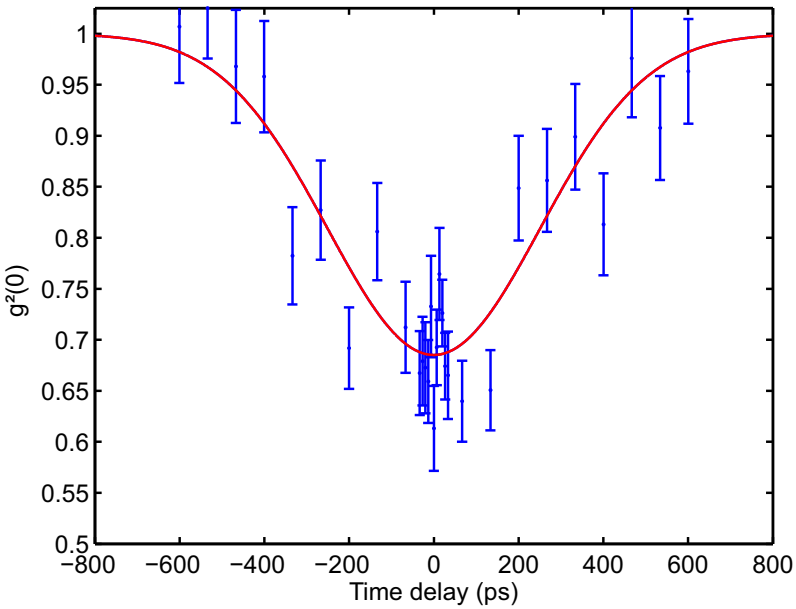

Figure 5.24: Measured two-photon interference of exciton photons from *dot5b* at sample #m649. The fit function is defined by: $P(\tau) = 1 - ae^{-\frac{x^2}{2b^2}}$. The parameters are $a = 0.31 \pm 0.03$ and $b = 250 \pm 40$ ps. Further details can be found in the text.

The shape of the overlapping wavepackets corresponds to the shape of the obtained Hong-Ou-Mandel dip. By measuring the coherence length of the exciton emission of *dot5b* one finds a gaussian instead of an expected exponential behaviour, indicating that there is a lot of noise in the exciton decay [34]. The Gausss fit yields a coherence length of $\tau_c = 174.4 \pm 3.7$ ps. Because of the Gaussian behaviour of the coherence measurement, we fitted a Gauss curve ($P(\tau) = 1 - ae^{-\frac{x^2}{2b^2}}$) to the obtained two-photon interference. The fit parameters are: $a = 0.31 \pm 0.03$ for the depth and $b = 250 \pm 40$ ps for the width of the dip. The lifetime of the exciton state of *dot5b* is not Fourier-limited ($2\tau_s/\tau_c = 7.3$, [34]). For a ratio equals 1 perfect two-photon interference is expected [39]. By embedding quantum dots into micropillars one can shorten the lifetime of certain states and therefore a better result without filtering the light can be achieved.

Chapter 6

Conclusions

In my thesis I presented various methods for a theoretical and experimental characterisation of quantum dots embedded in micropillars. The main results are the following:

1. We investigated the photoluminescence of over 3000 micropillars and presented the major results in this work.

2. We performed a measurement of the spectral reflectivity from the planar cavity sample #m649 with a white light source.

3. A theoretical simulation method for micropillar eigenmodes was developed during this thesis. The method is in good agreement with the experimental observed values, if the refractive indices of the materials are well known and a good knowledge of the dimensions of the system is provided.

4. By measuring the second-order correlation function we proved that quantum dots embedded in micropillars can produce nonclassical light. The two-photon excitation scheme presented in section 2.2.2 could improve the quality of auto-correlation measurements drastically. In practise this scheme can be applied only under angle excitation for micropillars with a clear exciton and biexciton signal.

5. We characterised cascade emission of quantum dots and measured a biexciton-exciton ratio of 10 % at sample C3281-13,7. The growth process of the InAs quantum dots is responsible for this low ratio, further investigations at the Unversity of Würzburg should improve this value.

6. We detected a weak Purcell enhancement by the factor of 1.5 of a quantum dot transition at micropillar sample C3281.

7. The effect of two-photon interference with resonant p-shell excitation was measured for *dot5b* at sample #m649 with a dip depth of 0.31 ± 0.03. Measuring two-photon interference from the emission of quantum dots in micropillars could lead to a better result, because of the shortened lifetime of quantum dot states on resonance.

Chapter 7

Outlook

The presented resonant two photon excitation scheme in chapter 2.2.2 was up to now only possible with one InAs quantum dot, *dot5b* from sample #m649. This scheme improves the purity of the biexciton and the exciton state drastically. One goal of our future work will be to show this resonant excitation also with quantum dots in micropillars.
Another project will be to show two-photon interference of dissimilar sources. For this we want to overlap photons from a quantum dot with photons from a spontaneous parametric down conversion source. The big challenge for showing the interference will be to produce photons with a high enough degree of indistinguishability.
For basic applications in quantum technology entangled photon pairs are very important. Therefore, projects in the future will be dealing with entanglement creation from semiconductor nanostructures.

Acknowledgements

Ich möchte die Chance nutzen, um ein großes **DANKE** an alle Leute, welche mich sowohl im Zusammenhang mit dieser Arbeit als auch in meinem privaten Leben unterstützt haben auszusprechen!

Für die fachliche Unterstützung und die gute Zusammenarbeit danke ich Allen aus der Photonik Forschungsgruppe der Universität Innsbruck. Danke Tobias für die unzähligen Erklärungen und für die Korrektur der Arbeit. Vielen Dank Benedikt für deine Geduld beim Programmieren. Weiters bedanke ich mich bei Gregor Weihs und Thorsten Schumm für die Möglichkeit an diesem Projekt mitzuarbeiten. Eure Faszination für Physik und Forschung hat mich immer sehr inspiriert.

Sowohl in Innsbruck als auch in Wien habe ich sehr nette Studienkollegen kennengelernt die mir mein Leben oft einfacher, schöner, spannender und lustiger gemacht haben. Danke für eure Freundschaft: Martina, Katrin, Bobby, Anda, Dani, Gregor, Michael S., Wolfgang, Tobias, Michi, Martin, Lorenz und Lukas... Ebenfalls möchte ich Gernot Grömer und dem Österreichischen Weltraumforum für die vielen spannenden Erlebnisse aus den letzten Jahren danken.
Vielen Dank an Alle von High Voltage für die vielen Partystunden und die schöne Zeit mit euch.

Danke Tutti, Harald, Mario, Mitch und Walter. Es freut mich immer wieder, dass ich mich auf euch verlassen kann und dass wir soviel Spass und Freude miteinander haben.
Liebe Tanja danke für die schönen Stunden die ich in den letzten zweieinhalb Jahren mit dir verbringen durfte und dafür dass du mir immer Mut gibst, wenn es manchal nicht so gut bei mir läuft.
Liebe Eltern, danke dass ihr nun seit über 26 Jahren immer für mich da seit wenn ich euch gebraucht habe und mir immer geholfen habt meine Träume zu verwirklichen.

Bibliography

[1] M. Planck. Über das Gesetz der Energieverteeilung im Normalspectrum. *Annnalen der Physik, 309(3):553563, 1901. ISSN 1521-3889. doi: 10.1002/andp.19013090310.*, 1900. [cited at p. 1]

[2] A. Einstein. Über einen die Erzeugung und Verwandlung des Lichtes betreffenden heuristischen Gesichtspunkt. *Annalen der Physik, 322(6):132148, 1905. ISSN 1521-3889. doi: 10.1002/andp.19053220607.*, 1905. [cited at p. 1]

[3] C. M. Santori. *Generation of nonclassical light using semiconductor quantum dots.* PhD thesis, Stanford University, 2003. [cited at p. 1, 4, 5, 6, 8, 9, 35, 46, 51]

[4] R. M. Stevenson, R. J. Young, P. Atkinson, K. Cooper, D. A. Ritchie, and A. J. Shields. A semiconductor source of triggered entangled photon pairs. *Nature*, 439(7073):179–182, January 2006. [cited at p. 1]

[5] C. H. Bennett and G. Brassard. Quantum cryptography: Public-key distribution and coin tossing. In *Proceedings of IEEE International Conference on Computer Systems and Signal Processing*, pages 175–179, New York, 1984. IEEE. [cited at p. 1]

[6] M. A. Nielsen and I. L. Chuang. *Quantum Computation and Quantum Information.* Cambridge University Press, Cambridge, 2000. [cited at p. 1]

[7] D. Bouwmeester, J.-W. Pan, K. Mattle, M. Eibl, H. Weinfurter, and A. Zeilinger. Experimental quantum teleportation. *Nature*, 390:575–579, 1997. [cited at p. 1]

[8] E. M. Purcell. Spontaneous emission probabilities at radio frequencies. *Phys. Rev.*, 69:681, Jun 1946. [cited at p. 1, 13, 16]

[9] G. Bryant and G. Solomon. *Optics of Quantum Dots and Wires.* Artech House, 2005. [cited at p. 3]

[10] M. S. Kushwaha. Plasmons and magnetoplasmons in semiconductor heterostructures. *Surface Science Reports*, 41(18):1 – 416, 2001. [cited at p. 3]

[11] P. Michler. *Single Quantum Dots*, volume 90, chapter Nonclassical Light from Single Semiconductor Quantum Dots, pages 315–347. Springer-Verlag, 2003. [cited at p. 4, 27, 28, 29, 45, 48]

[12] H. Drexler, D. Leonard, W. Hansen, J. P. Kotthaus, and P. M. Petroff. Spectroscopy of quantum levels in charge-tunable ingaas quantum dots. *Phys. Rev. Lett.*, 73:2252–2255, Oct 1994. [cited at p. 5]

[13] B. V. Shanabrook D. S. Katzer D. Gammon., E. S. Snow. and D. Park. Fine structure splitting in the optical spectra of single gaas quantum dots. *Physical Review Letters*, 1996, 1996. [cited at p. 6]

[14] Ioffe InAs Database, 2012. [cited at p. 7]

[15] T. Huber. Measurement and Modifcation of Biexciton-Exciton Time Correlation from an InAs Quantum Dot. Master's thesis, University of Innsbruck, Photoincs, 2011. [cited at p. 7, 33]

[16] R. Heitz, M. Grundmann, N. N. Ledentsov, L. Eckey, M. Veit, D. Bimberg, V. M. Ustinov, A. Y. Egorov, A. E. Zhukov, P. S. Kop'ev, and Zh. I. Alferov. Multiphonon-relaxation processes in self-organized inas/gaas quantum dots. *Applied Physics Letters*, 68(361), 1996. [cited at p. 8]

[17] A. Heinmki and A. Kapovits. Effect of doping and structural nonuniformities on reflectivity spectrum of alxga1-xas distributed bragg reflector. *Journal of Applied Physics*, 76(9):5429, 1994. [cited at p. 10]

[18] M. Born and E. Wolf. *Principle of Optics*. Pergamon Press, 6th edition, 1980. [cited at p. 10, 42]

[19] S. Gehrsitz, F. K. Reinhart, C. Gourgon, N. Herres, A. Vonlanthen, and H. Sigg. The refractive index of $Al_xGa_{1-x}As$ below the band gap: Accurate determination and empirical modeling. *Journal of Applied Physics*, 87(11):7825–7837, 2000. [cited at p. 10, 17, 23, 24, 42, 44]

[20] D. Burak and R. Binder. Cold-cavity vectorial eigenmodes of vcsels. *Quantum Electronics, IEEE Journal of*, 33(7):1205 –1215, jul 1997. [cited at p. 10, 17, 18, 19, 20, 21]

[21] J. M. Gerard, D. Barrier, J. Y. Marzin, R. Kuszelewicz, L. Manin, E. Costard, V. Thierry-Mieg, and T. Rivera. Quantum boxes as active probes for photonic microstructures: The pillar microcavity case. *Applied Physics Letters*, 69(4):449–451, 1996. [cited at p. 14]

[22] S. Reitzenstein and A. Forchel. Quantum dot micropillars. *Journal of Physics D: Applied Physics*, page 25, 2010. [cited at p. 14]

[23] T. Rivera and J. P. Debray. Optical losses in plasma-etched algaas microsresonators using reflection spectroscopy. *Appl. Phys. Lett.*, 911:74, 1999. [cited at p. 14, 15]

[24] D. Englund and J. Vučković. A direct analysis of photonic nanostructures. *Opt. Express*, 14(8):3472–3483, Apr 2006. [cited at p. 14]

[25] J. P. Reithmaier, G. Sek, A. Loffler, C. Hofmann, S. Kuhn, S. Reitzenstein, L. V. Keldysh, V. D. Kulakovskii, T. L. Reinecke, and A. Forchel. Strong coupling in a single quantum dot-semiconductor microcavity system. *Nature*, 432:197–200, November 2004. 10.1038/nature02969. [cited at p. 15]

[26] E. F. Schubert. Light-Emitting Diodes. *Cambridge university Press*, 2003. [cited at p. 15]

[27] L.A. Coldren and S.W. Corzine. *Diode lasers and photonic integrated circuits*. Wiley series in microwave and optical engineering. Wiley, 1995. [cited at p. 16]

[28] M. Pelton G. Solomon and Y. Yamamoto. Single-mode spontaneous emission from a single quantum dot in a three-dimensional microcavity. *Physical Review Letters*, 86.3903, 2000. [cited at p. 16]

[29] A. W. Snyder and J. D. Love. *Optical Waveguide Theory*. Chapman and Hall, London, 1991. [cited at p. 17, 18]

[30] B. E. A. Saleh and M. C. Teich. *Fundamentals of Photonics*. Wiley, 1991. [cited at p. 20]

[31] A. Yariv and P. Yeh. *Photonics: Optical Electronics in Modern Communication*. The Oxford Series in Electrical and Computer Engineering Series. Oxford University Press, 2007. [cited at p. 20]

[32] C. Schneider. Pre-characterization of sample c3281 and sample m4792. [cited at p. 21, 22, 23, 24, 25]

[33] R. Hanbury Brown and R. Q. Twiss. Correlation between photons in two coherent beams of light. *Nature*, 177:27, 1956. [cited at p. 29]

[34] T. Kauten. Towards Time-Bin Entangled Photons from Quantum Dots. Master's thesis, University of Innsbruck, 2012. [cited at p. 29, 52]

[35] D. Föger. Halbleiterquantenpunkte als Einzelphotonquellen. Bachelor's Thesis, July 2010. [cited at p. 45]

[36] A. Kiraz, S. Fälth, C. Becher, B. Gayral, W. V. Schoenfeld, P. M. Petroff, Lidong Zhang, E. Hu, and A. Imamoglu. Photon correlation spectroscopy of a single quantum dot. *Phys. Rev. B*, 65(16):161303, Mar 2002. [cited at p. 48]

[37] C. K. Hong, Z. Y. Ou, and L. Mandel. Measurement of subpicosecond time intervals between two photons by interference. *Phys. Rev. Lett.*, 59(18):2044, 1987. [cited at p. 49, 50]

[38] T. Schumm. *Two-Photon Interferometer - Manual*. TU-Vienna, 2011. [cited at p. 49]

[39] D. Santori, C.and Fattal, Jelena Vuckovic, Glenn S. Solomon, and Yoshihisa Yamamoto. Indistinguishable photons from a single-photon device. *Nature*, 419(6907):594–597, October 2002. [cited at p. 49, 52]